Monthly Notices
of the
ROYAL ASTRONOMICAL SOCIETY

Mon. Not. R. Astron. Soc. **405,** 1473–1490 (2010) doi:10.1111/j.1365-2966.2010.16560.x

Type III migration in a low-viscosity disc

Min-Kai Lin★ and John C. B. Papaloizou★

Department of Applied Mathematics and Theoretical Physics, University of Cambridge, Centre for Mathematical Sciences, Wilberforce Road, Cambridge CB3 0WA

Accepted 2010 February 19. Received 2010 January 19; in original form 2009 November 19

ABSTRACT

We study the type III migration of Saturn and Jupiter-mass planets in low-viscosity discs. A Saturn-mass planet is found to experience cyclic episodes of rapid decay in orbital radius, each amounting to a few Hill radii. We find this to be due to the scattering of large-scale vortices present in the disc. The origin and role of vortices in the context of type III migration is explored. It is shown through numerical simulations and semi-analytical modelling that spiral shocks induced by a sufficiently massive planet will extend close to the planet's orbital radius as well as being global prominent features. The production of vortensity across shock tips results in thin high vortensity rings with a characteristic width of the local scaleheight. For planets with masses equal to and above that of Saturn, the rings are co-orbital features extending all the way around the orbit. Linear stability analysis shows such vortensity rings are dynamically unstable. There exists unstable modes that are localized about local vortensity minima which coincide with gap edges. Simulations show that vortices are an outcome in the nonlinear regime.

We used hydrodynamic simulations to examine vortex–planet interactions. Their effect is present in discs with kinematic viscosity less than about an order of magnitude smaller than the typically adopted value of $\nu = 10^{-5}\Omega_{\rm p} r_{\rm p}(0)^2$, where $r_{\rm p}(0)$ and $\Omega_{\rm p}$ are the initial orbital radius and angular velocity of the planet, respectively. We find that the magnitude of viscosity affects the nature of type III migration but not the extent of the orbital decay. The role of vortices as a function of initial disc mass is also explored and it is found that the amount of orbital decay during one episode of vortex–planet interaction is independent of initial disc mass. We incorporate the concept of the co-orbital mass deficit in the analysis of our results and link it to the presence of vortices at gap edges. Similar effects are found to occur for a Jupiter-mass planet but with the extent of the fast migration episodes being larger because of the stronger perturbation on the disc.

Key words: planetary systems: formation – planetary systems: protoplanetary discs.

1 INTRODUCTION

The importance of planet migration was realized with the discovery of the first exoplanet with an orbital period of 4 d (Mayor & Queloz 1995). Such planets, classified as 'hot Jupiters', orbit so close to their host stars that it is difficult to understand their formation *in situ*. It is thought they form further out then migrate inwards due to torques from the gaseous protoplanetary disc.

Tidal interactions between a protoplanet and protoplanetary disc were in fact studied well before observations of exoplanets (Goldreich & Tremaine 1979, 1980). In these early studies, the protoplanet is treated as a small perturbation, the linearized hydrodynamic equations are then solved for the disc response. Density waves launched at Lindblad resonances generally lead to decay of the planet's semimajor axis. This scenario is referred to as type I migration (Ward 1997). Recent semi-analytical treatments include Tanaka, Takeuchi & Ward (2002) for isothermal discs and Paardekooper et al. (2010) for a non-isothermal equation of state. For planet masses above that of Jupiter, linear theory ceases to apply and the non-linear disc response produces a surface density gap about the planet (Lin & Papaloizou 1986). In this migration mode, now called type II, the planet's orbital radius is locked with the disc viscous evolution. That is, it drifts towards the central star along with disc material, while residing inside the gap.

Recently, a new migration mode, called runaway or type III migration, was introduced by Masset & Papaloizou (2003) and further

★E-mail: mkl23@cam.ac.uk (M-KL); J.C.B.Papaloizou@damtp.cam.ac.uk (JCBP)

discussed by Artymowicz (2004a) and Papaloizou (2005). Type III migration is a self-sustaining mechanism with short migration time-scales $\leq O(10^2)$ orbits. A series of detailed numerical studies was presented by Pepliński, Artymowicz & Mellema (2008a,b,c), who considered a Jupiter-mass planet and included thermal effects and corrections for self-gravity (SG). They found that for a range of surface density profiles that were non-decreasing inwards, that provided the disc was massive enough, the planet's semimajor axis was reduced by a factor of between 2.5 and ∼3 within time of 40–60 orbital periods. They noted that this type III migration is strongly dependent on the flow inside the Hill radius of the planet.

Type III migration is also applicable to intermediate-mass planets comparable to Saturn in massive discs. The planet opens a partial gap which, in the case of a migrating planet, allows a net drift of disc material across the planet's orbital radius through executing U-turns at the end of horseshoe orbits. The change in the fluid elements' orbital radius implies a torque on the planet that is proportional to its migration rate. The migration rate also increases with the co-orbital mass deficit δm, which is proportional to the difference between surface density of the co-orbital region and that of the orbit-crossing flow.

Most previous disc–planet simulations have either included a large enough applied viscosity or had enough numerical diffusion to suppress instabilities resulting in a smooth behaviour. For example, the studies of Pepliński et al. (2008a,b,c) did not display instabilities even with no applied physical viscosity. However, they employed a Cartesian grid-based code (FLASH) which is indicated through studies undertaken by de Val-Borro et al. (2007) to have too much numerical diffusion to allow steep enough gradients to form and subsequently become unstable.

In this work, we study a modified form of type III migration, which is non-smooth, induced by large-scale vortices originating from instabilities. The vortex forms outside the Hill sphere and flows across the co-orbital region. Changing the gravitational softening length applied to the planet potential, or adopting the equation of state of Pepliński et al. (2008a), which modifies flow inside the Hill sphere, is found not to significantly affect the vortex–planet interaction described in this paper.

The linear theory of instabilities in inviscid accretion discs associated with ring structures, sharp edges and vortensity extrema is well known (Papaloizou & Pringle 1984; Papaloizou & Lin 1989; Lovelace et al. 1999; Li et al. 2000) and vortices develop in the nonlinear regime (Li et al. 2001). In the context of protoplanetary discs, steep gradients arise from gap edges associated with sufficiently massive planets. de Val-Borro et al. (2007) performed simulations of a Jupiter-mass planet held on fixed orbit to show the formation of large-scale vortices at gap edges. The migrating case was considered by Ou et al. (2007) for a Neptune-mass planet. The authors find non-smooth migration associated with non-axisymmetric surface density enhancements near the gap edge. In this paper, we examine this effect in more detail for a Saturn-mass planet undergoing type III migration.

This paper is organized as follows. Section 2 describes the set of equations that we used to model the disc–planet system and in Section 3 we describe the formation of vortensity rings using numerical simulations and a semi-analytical model. We then study their dynamical stability in Section 4. In Section 5, we present hydrodynamic simulations of type III migration as a function of viscosity, highlighting the effect of vortices at low viscosity. We analyse the inviscid case in detail in Section 6 and the effects of varying the disc mass as well as the type III migration of a Jupiter-mass planet. Finally in Section 7 we summarize our results.

2 BASIC EQUATIONS AND MODEL

We consider a planet of mass M_p orbiting a central star of mass M_*. We adopt a cylindrical coordinate system (r, ϕ, z) where z is the vertical coordinate increasing in the direction normal to the disc plane for which the unit vector is $\hat{\boldsymbol{k}}$. We integrate vertically to obtain a 2D flat disc model, for which the governing hydrodynamic equations in a frame uniformly rotating with angular velocity $\Omega_\mathrm{p}\hat{\boldsymbol{k}}$ are the continuity equation

$$\frac{\mathrm{D}\Sigma}{\mathrm{D}t} = -\Sigma\nabla\cdot\boldsymbol{u}, \tag{1}$$

and the equation of motion

$$\frac{\mathrm{D}\boldsymbol{u}}{\mathrm{D}t} + 2\Omega_\mathrm{p}\hat{\boldsymbol{k}}\wedge\boldsymbol{u} = -\frac{1}{\Sigma}\nabla P - \nabla\Phi_\mathrm{eff}, \tag{2}$$

where $\mathrm{D}/\mathrm{D}t$ is the total derivative and the vertically integrated pressure $P = c_s^2(r)\Sigma$ with $c_s = h(GM_*/r)^{1/2}$. Here, Σ is the surface density, $\boldsymbol{u}$ is the velocity and the effective gravitational and centrifugal potential is given by

$$\begin{aligned}\Phi_\mathrm{eff} = &-\frac{GM_*}{r} - \frac{GM_\mathrm{p}}{\sqrt{r^2 + r_\mathrm{p}^2 + 2rr_\mathrm{p}\cos(\phi-\phi_\mathrm{p}) + \epsilon^2}} \\ &- \frac{1}{2}\Omega_\mathrm{p}^2 r^2 + \frac{GM_\mathrm{p}}{r_\mathrm{p}^2}\cos(\phi-\phi_\mathrm{p}) \\ &+ r\int \frac{G\Sigma(r',\phi')}{r'^2}\cos(\phi-\phi')r'\mathrm{d}r'\mathrm{d}\phi'\end{aligned} \tag{3}$$

(Masset 2002). The last two terms on right-hand side (RHS) are indirect terms accounting for acceleration of the primary. In the above, the cylindrical coordinates of the planet that is confined to remain in the disc plane are $(r_\mathrm{p}, \phi_\mathrm{p}, 0)$ and the softening length $\epsilon = 0.6H(r_\mathrm{p})$, where $H(r) = hr$ is called the disc semithickness as it would correspond to this quantity if the vertical structure is considered, and $h = 0.05$ is the related constant aspect ratio. Although the numerical and analytical work is based on the 2D equations, ϵ may be regarded as accounting for the effect of the vertical stratification on the vertically averaged potential calculation.

2.1 Vortensity conservation

The vortensity being the ratio of the z component of the vorticity (hereafter just called the vorticity, ω) to the surface density is defined to be

$$\eta = \frac{\omega}{\Sigma} \equiv \frac{\omega_r + 2\Omega_\mathrm{p}}{\Sigma}, \tag{4}$$

where $\omega_r = \hat{\boldsymbol{z}}\cdot\nabla\wedge\boldsymbol{u}$ is the relative vorticity seen in the rotating frame. It is well known that in barotropic flows without shocks it follows from (1) and (2) that the vortensity $\eta = \omega/\Sigma$ is conserved for a fluid particle. When an isothermal equation of state with variable sound speed as is used here is adopted, vortensity is no longer strictly conserved. However, the sound speed varies on a global scale so that when phenomena are considered on a local scale vortensity is conserved to a good approximation in the absence of shocks.

2.2 Hydrodynamic simulations

Our work is based on numerical simulations and specific parameters depend on the problem at hand, as is described in the following sections. Here, we present the general set up.

For convenience, we adopt dimensionless units such that the orbital radius of the planet, $r_p(t)$, is initially $r_p(0) = 2$. Time is expressed in units of the initial orbital period $P_0 = 2\pi/\Omega_p$, where $\Omega_p = \sqrt{GM_*/r_p^3(0)}$ is the planet's initial Keplerian angular velocity. The unit of mass is taken to be the central mass M_* which for working purposes may be considered to be $1\,M_\odot$. The disc has an initially uniform surface density $\Sigma = \Sigma_0 \times 10^{-4}$ with Σ_0 being a dimensionless constant taken to be in the interval [1, 9]. Some simulations include a constant kinematic viscosity $\nu = \nu_0 \times 10^{-5}$ in physical units of $r_p^2(0)\Omega_p$, with ν_0 being a dimensionless constant with values taken to be in the interval [0, 1].

We use the FARGO code to solve for the disc response (Masset 2000a,b).FARGO evolves the hydrodynamic equations in global cylindrical co-ordinates centred on the central object. We used a non-rotating frame for the simulations described here. Indirect terms arising from the non-inertial frame are included in the potential. The code uses a finite-difference scheme with van Leer upwind advection, similar to the ZEUS code (Stone & Norman 1992) but it employs a modified algorithm for azimuthal transport that allows for large time-steps. We take 2π-periodic boundary condition in azimuth and wave-damping boundary conditions at disc boundaries (de Val-Borro et al. 2006). We remark that vortensity ring formation occurs as a result of shocks near the planet and therefore is unaffected these boundary conditions.

In cases where the planet is allowed to migrate, a fifth order Runge-Kutta method incorporated in FARGO was used to integrate its equation of motion. The accuracy of this is governed by the simulation time-step which decreases in proportion with the resolution which also determines the accuracy of the gravitational force calculation. It is accordingly checked with the rest of the scheme by increasing resolution. For our simulations this was varied by a factor of four. We also ran simulations at the same resolution with halved time-step. We found that simulation results were not affected. In particular, the extent of planet migration induced by vortex scattering and the number of scattering events was found to be the same. Thus, we believe the Runge–Kutta integrator is sufficiently accurate to capture the orbital evolution.

3 RING STRUCTURES IN DISC–PLANET INTERACTIONS

In this section, we present hydrodynamic simulations to show that narrow surface density rings are brought about as a consequence of the fact that highly peaked vortensity (being the ratio of the vorticity to the surface density) rings are produced by flow through quasi-steady shocks located close to the planet. For sufficiently massive planets, the associated vortensity generation occurs as fluid elements execute a horseshoe turn in the co-orbital region. Focusing on such cases, we construct a simple model that enables an estimate of the shock location to be made together with rate of the vortensity generation as material flows through it. Our model is in good agreement with numerical simulations and confirms the process of vortensity generation within a planet's co-orbital region which later plays an important role in modifying the flow structure there.

3.1 Vortensity generation by the shocks induced by a Saturn-mass planet

We first consider the case with $M_p = 2.8 \times 10^{-4} M_*$ corresponding to a Saturn-mass planet around a solar-mass star. Here, the planet potential is switched on gradually over a time $5P_0$. The computation

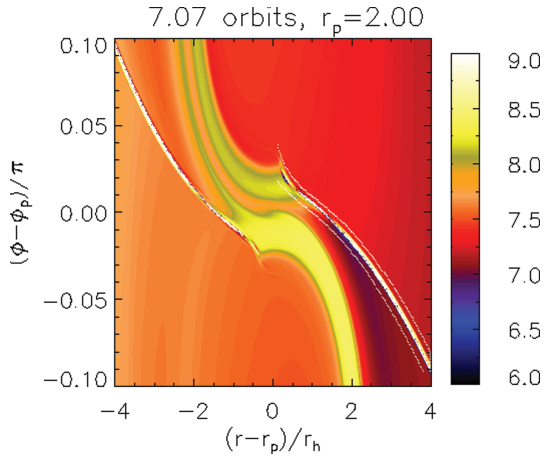

Figure 1. Vortensity generation and destruction across shocks induced by a Saturn-mass planet in an inviscid disc. The plot shows $\ln\eta = \ln(\omega/\Sigma)$. Regions of increased vortensity are clearly visible as half horseshoes above and below the planet. The increase occurs as material passes through parts of the shock fronts that extend into the co-orbital region.

domain is $r = [1, 3]$ and the resolution was $N_r \times N_\phi = 1024 \times 3072$, corresponding to radial and azimuthal grid spacings of $\Delta r \simeq 0.02 r_h$ and $r\Delta\phi \simeq 0.05 r_h$, respectively, where $r_h = [M_p/(3M_*)]^{1/3} r_p$ is the planet's Hill radius. The planet is held on fixed circular orbit and the disc has density $\Sigma_0 = 1$ with no explicit viscosity ($\nu = 0$).

Fig. 1 shows the vortensity field at $t = 7.07$ close to the planet. Vortensity is generated/destroyed as material passes through the two spiral shocks. For the outer shock, vortensity generation occurs for fluid elements executing a horseshoe turn ($|r - r_p| \lesssim r_h$) while vortensity is reduced for fluid that passes by the planet, but the change is smaller in magnitude in the latter case. The situation is similar for the inner shock, but some post-shock material with increased vortensity continues to pass by the planet. This stream begins at $r \simeq -r_h$ but such feature is absent at the outer shock, suggesting a lack of symmetry about $r = r_p$, possibly resulting from the non-uniform vortensity background being $\propto r^{-3/2}$. Note that although a pre-shock fluid element that would be on a horseshoe trajectory may in fact pass by the planet after crossing the shock, it is clear that vortensity rings originate from passage through shock fronts interior to the co-orbital region that would correspond to the horseshoe region for free particle motion.

The streams of high vortensity eventually move around the whole orbit outlining the entire co-orbital region. Fig. 1 shows that they are generated along a small part of the shock front of length $\sim r_h$. This results in thin rings with a similar radial width. The fact that they originate from horseshoe material can enhance the contrast as post-shock inner disc horseshoe material is mapped from $r - x$ to $r + x$ to become adjacent to post-shock outer disc material passing by the planet.

We also show in Fig. 2 long-term evolution of average co-orbital properties from a corresponding low-resolution run ($N_r \times N_\phi = 256 \times 768$). The co-orbital region is taken to be the annulus $[r_p - x_s, r_p + x_s]$. We fix $x_s = 2.5 r_h$, as is typically measured from hydrodynamic simulations (Artymowicz 2004b; Paardekooper & Papaloizou 2009) for intermediate or massive planets. In Appendix A we show that in the particle dynamics limit $x_s \lesssim 2.3 r_h$, comparable to the value adopted above.

Vorticity generation occurs within $t \lesssim 25$ orbits, after which it remains approximately steady. For a Jupiter-mass planet, the time taken to reach the corresponding state is about 50 orbits, but most

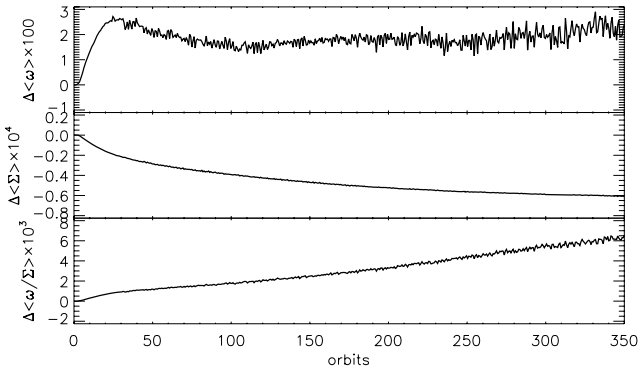

Figure 2. Long-term evolution of co-orbital properties for a Saturn-mass planet held on fixed orbit. Vorticity, density and vortensity perturbations are expressed relative to their values at $t = 0$. Angle brackets denote a spatial average over the co-orbital region defined by the annulus $r = [r_\mathrm{p} - 2.5r_\mathrm{h}, r_\mathrm{p} + 2.5x_s]$.

of the vorticity generation also occurs in the first ∼25 orbits. It is important to note that subsequent vortensity increases occur in narrow rings with fluctuations being due to instabilities associated with them. The average surface density falls more gently as the planet opens a gap, which is a requirement for the rings to be self-supported. Consequently, we observe a rise in co-orbital vortensity. Fig. 2 reflects modification of co-orbital properties on dynamical time-scales due to shocks, so we expect migration mechanisms which depend on co-orbital structure to be affected.

3.2 Location of the vortensity generation region for different planet masses

The process of formation of vortensity rings discussed here differs from that observed in Koller, Li & Lin (2003) and Li et al. (2005), where the rings are generated by shocks outside the co-orbital region. This is because the authors used a smaller planet mass. To illustrate the effect of reducing the mass, we ran simulations with $N_r \times N_\phi = 256 \times 768$ for $M_\mathrm{p} \times 10^4 = 1$, 2.8 and 10. Fig. 3 compares azimuthally averaged vortensity perturbations induced in each case after 14.14 orbits. The intermediate- and high-mass cases are qualitatively similar, having $\Delta(\omega/\Sigma)$ maxima at $r - r_\mathrm{p} \sim \pm 2r_\mathrm{h}$ and minima at $r - r_\mathrm{p} \sim 3r_\mathrm{h}$. The magnitude of $\Delta(\omega/\Sigma)$ increases with M_p because higher masses induce higher Mach number shocks. As the half-width of the horseshoe region is $x_s = 2.5r_\mathrm{h}$ for such masses, vortensity rings are co-orbital features.

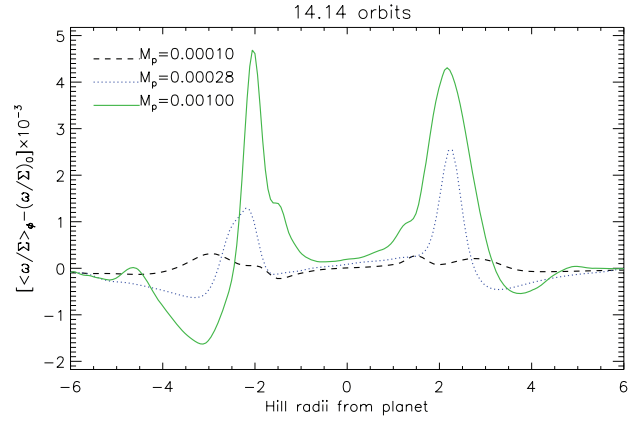

Figure 3. Azimuthally averaged vortensity perturbation for different planet masses.

The low-mass $M_\mathrm{p} = 10^{-4}$ case has much smaller $|\Delta(\omega/\Sigma)|$. There is a vortensity maximum at $r - r_\mathrm{p} = -3r_\mathrm{h}$ but nothing of similar magnitude at $r - r_\mathrm{p} > 0$. Paardekooper & Papaloizou (2009) found the co-orbital half-width, in the limit of zero softening for low-mass planets, to be

$$x_s = 1.68(M_\mathrm{p}/h)^{1/2} r_\mathrm{p}. \tag{5}$$

For $M_\mathrm{p} = 10^{-4}$, $h = 0.05$, $x_s = 2.33r_\mathrm{h}$. Non-zero softening gives a smaller x_s. Hence, vortensity rings for low-mass planets occur outside the co-orbital region as is confirmed in our simulations and they are very much weaker.

3.3 A semi-analytic model for co-orbital vortensity generation by shocks

We now construct a semi-analytic model describing the process of shock-generation of vortensity. In this way, we gain an understanding of the physical processes involved and later how they lead to strong torques and fast migration of the planet and under what conditions simulations can represent them accurately.

More specifically, we model the outer spiral shock in Fig. 1. To do this, we need the pre-shock flow field, the shock front location and then to evaluate the vortensity change undergone by material as it passes through the shock. We now consider these in detail.

3.3.1 Flow field

We first simplify the geometry by adopting the shearing box approximation (e.g. Paardekooper & Papaloizou 2009). As we are concerned with the flow near the planet, we consider a local Cartesian co-ordinate system (x, y) co-rotating with the planet at angular speed Ω_p and with origin at its centre of mass. Without the planet, the velocity field is Keplerian $\boldsymbol{u} = (0, -3\Omega_\mathrm{p}x/2)$. In order to deal with the pre-shock flow, we make the assumption that pressure effects can be ignored when compared to the planet potential. This ballistic approximation is appropriate for a slowly varying supersonic flow as is expected to be appropriate for the pre-shock fluid. The velocity $\boldsymbol{u}$ satisfies the local form of equation (2) with $P = 0$ and the effective potential

$$\Phi_\mathrm{eff} = -\frac{GM_\mathrm{p}}{\sqrt{x^2 + y^2 + \epsilon^2}} - \frac{3}{2}\Omega_\mathrm{p}^2 x^2 \tag{6}$$

and thus follows from particle dynamics. The indirect terms are neglected in this approximation. We write a fluid particle's trajectory in a steady-state flow in the form of $x = x(y)$ and the corresponding velocity field as $\boldsymbol{u} = \boldsymbol{u}(y)$. Noting that on a particle trajectory we have $\frac{\mathrm{D}}{\mathrm{D}t} = u_y \frac{\mathrm{d}}{\mathrm{d}y}$, it follows from the local form of (2) that on a particle trajectory we have the following system of three simultaneous first-order differential equations:

$$\frac{\mathrm{d}u_y^2}{\mathrm{d}y} = -4\Omega_\mathrm{p} u_x - \frac{2M_\mathrm{p} y}{(x^2 + y^2 + \epsilon^2)^{3/2}} \equiv Q, \tag{7}$$

$$\frac{\mathrm{d}}{\mathrm{d}y}\left(u_x u_y^2\right) = u_y\left[3\Omega_\mathrm{p}^2 x - \frac{M_\mathrm{p} x}{(x^2 + y^2 + \epsilon^2)^{3/2}}\right] + u_x Q + 2\Omega_\mathrm{p} u_y^2, \tag{8}$$

$$\frac{\mathrm{d}}{\mathrm{d}y}\left(x u_y^2\right) = xQ + u_x u_y. \tag{9}$$

We use these to solve for the state vector $\boldsymbol{U}(y) = [u_y^2,\ u_x v_y^2,\ x u_y^2]$ in $x > 0$ for a particular particle. The boundary condition is

$$(u_y,\ u_x,\ x) \to (-3\Omega_\mathrm{p} x_0/2,\ 0,\ x_0) \text{ as } y \to \infty, \tag{10}$$

where $x = x_0$ is the particle's unperturbed path. The totality of paths obtained by considering a continuous range of x_0 then constitutes the flow field. Having obtained the velocity field, we use vortensity conservation to obtain Σ. The surface density is then

$$\Sigma(x, y) = \frac{2\Sigma_0}{\Omega_\mathrm{p}}(\omega_r + 2\Omega_\mathrm{p}), \tag{11}$$

where the unperturbed absolute vorticity is $\omega = \Omega_\mathrm{p}/2$. Numerically, we calculated the relative vorticity by relating it to the circulation through

$$\omega_r \simeq \frac{1}{\Delta A}\oint \boldsymbol{u}\cdot \mathrm{d}\boldsymbol{l}, \tag{12}$$

where the integration is taken over a closed loop about the point of interest and ΔA is the enclosed area. This avoids errors due to numerical differentiation on the uneven grid in (x, y) generated by solving the above system.

3.3.2 *Location of the shock front*

The physical reason for shock formation is the fact that the planet presents an obstacle to the flow. Where the relative flow is subsonic, the presence of this obstacle can be communicated to the fluid via sound waves emitted by the planet. In regions where the relative flow is supersonic, the fluid is unaware of the planet via sound waves (but the planet's gravity is felt). We estimate the location of the boundary separating these two regions by specifying an appropriate characteristic curve or ray defining a sound wave. This is a natural location for shocks. Applying this idea to Keplerian flow, Papaloizou, Nelson & Snellgrove (2004) obtained a good match between the predicted theoretical shock front and the wakes associated with a low-mass planet. For general velocity field $\boldsymbol{u}$, the characteristic curves satisfy the equation

$$\frac{\mathrm{d}y_s}{\mathrm{d}x} = \frac{\hat{u}_y^2 - 1}{\hat{u}_x\hat{u}_y - \sqrt{\hat{u}_x^2 + \hat{u}_y^2 - 1}}, \tag{13}$$

where $\hat{u}_i = u_i/c_s$. The positive sign of the square root has been chosen so that the curves have negative slope in the domain $x > 0$ with $u_y < 0$. As the fluid flows from super-sonic ($y > y_s$) to subsonic ($y < y_s$), fluid located at $y = y_s$ begins to know about the planet through pressure waves (Papaloizou et al. 2004). In Keplerian flow, the rays defining the shock fronts originate from the sonic points at $x = \pm 2H/3$, $y = 0$. In a general flow, sonic points where $|\boldsymbol{u}| = c_s$, at which the rays may start, lie on curves and can occur for $x < 2hr_\mathrm{p}/3$. The starting sonic point for solving equation (13) that we eventually adopted has $x = 0$ and the value of $y > 0$ that is furthest possible from the planet.

3.3.3 *Vorticity and vortensity changes across a shock*

The jump in absolute vorticity $[\omega]$ is readily obtained by resolving the fluid motion parallel and perpendicular to the shock front (e.g. Kevlahan 1997). As we do not solve the energy equation, shocks are locally isothermal and our expression differs from those of Kevlahan (1997), accordingly a brief derivation of $[\omega]$ is presented in Appendix B. The result for a steady shock is

$$[\omega] = -\frac{(M^2-1)^2}{M^2}\frac{\partial u_\perp}{\partial S} + (M^2-1)\omega - \left(\frac{M^2-1}{u_\perp}\right)\frac{\partial c_s^2}{\partial S}, \tag{14}$$

where $u_\perp$ is the pre-shock velocity component perpendicular to the shock front, $M = u_\perp/c_s$ is perpendicular Mach number and $c_s = hr^{-1/2}$ is the sound speed. $\partial/\partial S$ is the derivative along the shock. It is important to note that for (14) to hold, the direction of increasing S, the direction of positive $u_\perp$ and the vertical direction should form a right-handed triad. We take increasing S as moving away from the planet. The local isothermal equation of state produces the last term on RHS of equation (14). Because of the slow variation of c_s, its contribution is not important in this application.

The vortensity jump $[\omega/\Sigma]$ follows immediately from equation (14) as

$$\left[\frac{\omega}{\Sigma}\right] = -\frac{(M^2-1)^2}{\Sigma M^4}\frac{\partial u_\perp}{\partial S} - \left(\frac{M^2-1}{\Sigma M^2 u_\perp}\right)\frac{\partial c_s^2}{\partial S}, \tag{15}$$

which essentially reduces to the expression derived by Li et al. (2005) if c_s = constant (and a sign change due to different convention). The sign of $[\omega/\Sigma]$ depends mainly on the gradient of $u_\perp$ (or M) along the shock. As in our case $u_\perp < 0$, the width of the increased vortensity rings produced is determined by the length along the shock where $|M|$ is increasing. Note that $[\omega/\Sigma]$ does not depend explicitly on the pre-shock vortensity, unlike the absolute vorticity jump.

3.3.4 *Comparison of the results of the semi-analytic model with numerical simulations*

We now compare the results of hydrodynamic simulations with those obtained from the model. First, we illustrate the particle paths that constitute the flow field together with the shock fronts obtained by assuming coincidence with the characteristic curves that are obtained from the semi-analytic model in Fig. 4. A polynomial fit to the simulation shock front is also shown. Particle paths cross for

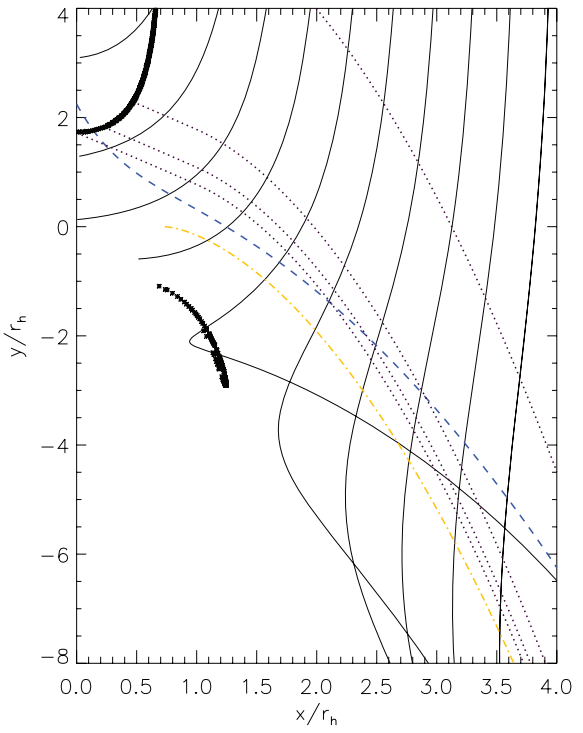

Figure 4. Solid lines: particle paths from the reduced zero-pressure momentum equations (equations 7–9); thick lines: curves composed of sonic points on which $|\boldsymbol{u}| = c_s$; dotted lines: theoretical shock fronts; dash–dotted line: solution to equation (13) for Keplerian flow; dashed line: polynomial fit to simulation shock front. The actual shock front begins at a sonic point around $x = 0.2r_\mathrm{h}$.

$x > r_h$, $y < -2r_h$ so that the neglect of pressure becomes invalid. Accordingly, the solution to equation (4) should not be trusted in this region. Fortunately, vortensity generation occurs at a distance from the planet that is within r_h, where pre-shock particle paths do not cross.

In Fig. 4, the estimated shock location is qualitatively good and tends to the Keplerian solution further away. The important feature is that the shock can extend close to $x = 0$, across horseshoe orbits. If the flow were purely Keplerian, there could be no significant vortensity generation close to $x = 0$ because the flow becomes subsonic there. Furthermore, only circulating fluid can be shocked in that case. Shock generation of vortensity inside the co-orbital region is only possible for sufficiently massive planets that induce large enough non-Keplerian velocities.

The key quantity determining vortensity generation is the perpendicular Mach number. Fig. 5 compares M from simulation and model. Although the semi-analytic model gives a shock Mach number that is somewhat smaller than that found from the simulation, all curves have $|M|$ increasing from $x = 0 \rightarrow 1.3r_h$ which is the important domain for vortensity generation. Thus, equation (15) implies vortensity generation in all cases. Fig. 6(a) illustrates various combinations of semi-analytic modelling and simulation data that have been used to estimate the vortensity jump across the shock. The qualitative similarities between the various curves confirms that vortensity generation occurs within co-orbital material about 1 Hill radius away from the planet. It is shocked as it undergoes horseshoe turns.

Assuming that material is mapped from $x \rightarrow -x$ as it switches to the inner leg of its horseshoe orbit, we expect the outer spiral shock to produce a vortensity ring peaked at $r - r_p \sim -0.5r_h$ of width O(r_h) [= O(H)], with a similar discussion applying to the inner shock which is expected to produce a vortensity ring peaked at $r - r_p \sim 0.5r_h$. Of course, as a fluid element moves away from the U-turn region, $|r - r_p|$ increases, but it remains on a horseshoe orbit. Thus, thin vortensity rings are natural features of the co-orbital region for such planet masses.

We have also tested our model for $M_p = 2 \times 10^{-4}$ in Fig. 6(b). There is still a good qualitative match between the simulation and the model; even though lowering M_p makes the zero-pressure approximation, adopted to determine the semi-analytic flow field, less good. Decreasing M_p shifts vortensity generation away from the planet in the semi-analytic model, as is also observed in the hydrodynamic simulation (Fig. 3). In this case, there is no vortensity generation in $r - r_p < 0.5r_h$ but vortensity rings are still co-orbital (with peaks at $\sim 0.7r_h$).

We remark that steep vortensity gradients are associated with dynamical instabilities (e.g. Papaloizou & Pringle 1985) and this is explored in more detail below.

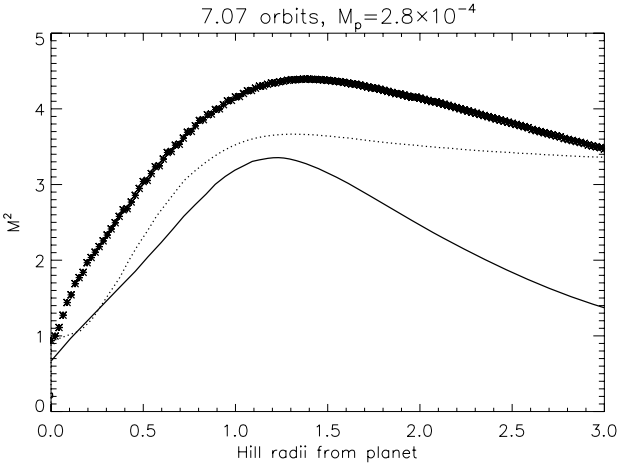

Figure 5. Perpendicular Mach number squared M^2 along the outer spiral shock illustrated in Fig. 1. Asterisks: simulation data; dotted line: M^2 obtained from the simulation shock and the semi-analytic flow; solid line: M^2 obtained from the semi-analytic shock front and flow.

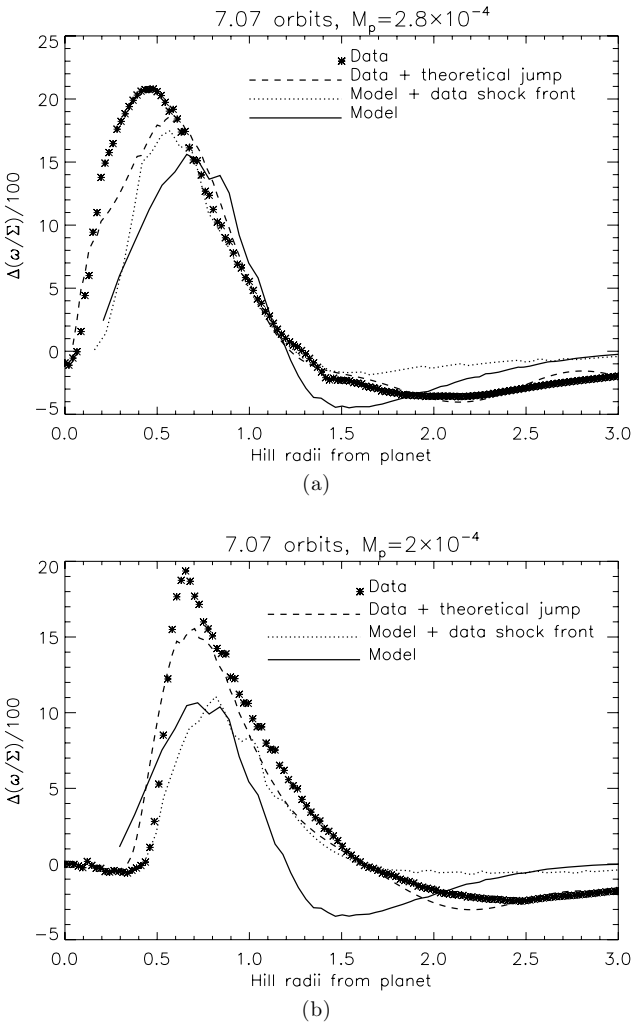

Figure 6. Semi-analytic and actual vortensity jumps across a shock in the co-orbital region. Asterisks are measured from the simulations. The dashed lines were obtained by using pre-shock simulation data coupled with the jump condition specified by equation(15). The dotted lines were obtained using the semi-analytic flow field together with the location of the shock front obtained from the simulation. The solid curves correspond to the semi-analytic model for both the flow field and shock front.

4 DYNAMICAL STABILITY OF VORTENSITY RINGS

Having established the origin of the vortensity rings and the mechanism for producing them, we go on to study the linear stability of the shock-modified protoplanetary disc model described above. This is an important issue as instability can lead to their breaking up into mobile non-axisymmetric structures which can affect the migration of the planet significantly.

The linear stability of inviscid barotropic axisymmetric rings and discs without a planet is well developed (Papaloizou & Pringle 1984, 1985; Papaloizou & Lin 1989). The extension to a non-barotropic equation of state was undertaken more recently (Lovelace et al. 1999; Li et al. 2000). This work indicates that sharply peaked surface density or vortensity features in the disc are associated with dynamical instabilities. It is directly relevant to the types of configuration that we have found to be produced by the disc planet interactions described above. For example, de Val-Borro et al. (2007) considered the linear instability of gap edges associated with a Jupiter-mass planet and connected it to vortex formation there.

Here, we consider the stability of the partial gap opened by a Saturn-mass planet, for which type III migration is expected in a massive disc. In order to be able to do, this we need to be able to define an appropriate background equilibrium axisymmetric structure to perturb. We show that this is possible.

4.1 Basic background state

The basic state should be axisymmetric and time independent with no radial velocity ($\partial/\partial\phi = \partial/\partial t = u_r = 0$). To set this up, we suppose the vortensity profile $\eta(r)$ is known (e.g. via shock modelling as above) and that accordingly we have

$$\eta(r) = \frac{1}{r\Sigma}\frac{\mathrm{d}}{\mathrm{d}r}(r^2\Omega). \tag{16}$$

The radial momentum equation gives

$$r\Omega^2 = \frac{1}{\Sigma}\frac{\mathrm{d}P}{\mathrm{d}r} + \frac{GM_*}{r^2}. \tag{17}$$

Using these together with the locally isothermal equation of state, $P = h^2 GM_*\Sigma/r$, h being the constant aspect ratio, we obtain a single equation for Σ in the form

$$h^2\frac{\mathrm{d}^2\ln\Sigma}{\mathrm{d}r^2} = \frac{h^2-1}{r^2} + \frac{2\Sigma\eta}{\sqrt{GM_*}}\left(\frac{1-h^2}{r} + h^2\frac{\mathrm{d}\ln\Sigma}{\mathrm{d}r}\right)^{1/2} - \frac{2h^2}{r}\frac{\mathrm{d}\ln\Sigma}{\mathrm{d}r}. \tag{18}$$

We solve equation (18) for Σ with $\eta(r)$ taken as an azimuthal average from the fiducial simulation described in (Section 3.1) at a time at which vortensity rings have developed. These structures are essentially axisymmetric apart from in the close neighbourhood of the planet. They are illustrated in Fig. 7. The boundary conditions is $\Sigma = \Sigma_0 = 1$ at $r = 1.1$, and $r = 3$. These conditions are consistent with the fact that shock modification of the surface density profile only occurs near the planet ($r = 2$).

A comparison between hydrostatic surface density and angular velocity profiles obtained by solving equation (18) with those obtained as azimuthal averages from the corresponding simulation is illustrated in Fig. 8(a) and (b). The agreement is generally very good indicating that the adoption of the basic axisymmetric state defined by the simulation vortensity profile, together with equation (17), for stability analysis should be a valid procedure. Fig. 8(a) shows that vortensity rings reside in the horseshoe region just inside the gap. At a surface density extrema, equation (18) implies that

$$h^2\frac{\mathrm{d}^2\ln\Sigma}{\mathrm{d}r^2} = \frac{h^2-1}{r^2} + 2\Sigma\eta\sqrt{\frac{1-h^2}{GM_*r}}.$$

Since $h \ll 1$, if η is sufficiently large then $\mathrm{d}^2\Sigma/\mathrm{d}r^2 > 0$. Hence, vortensity maxima will coincide with surface density minima. In our basic state, local minima and maxima are separated by O(H) ($\simeq$0.1). As vortensity rings originate from spiral shocks,

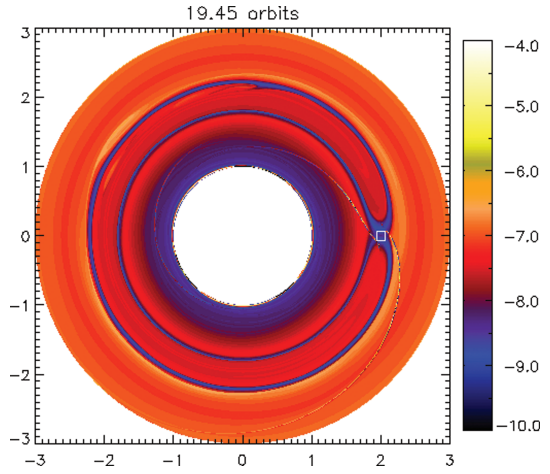

Figure 7. A contour plot of $\ln(\Sigma/\omega)$ when the vortensity ring like structures have formed in the co-orbital region. These are almost axisymmetric apart from in the region very close to the planet. The centre of the small square marks the planet position.

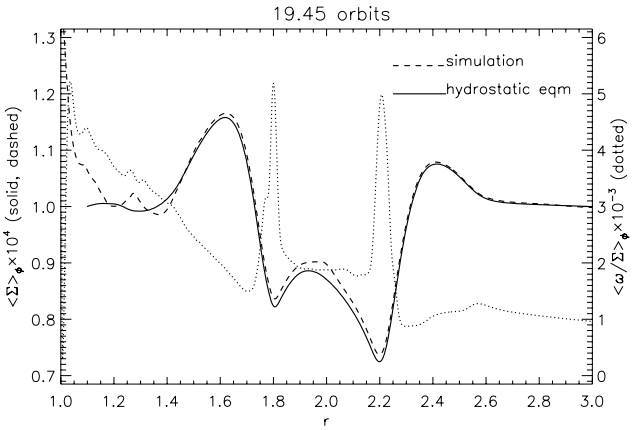

(a) Σ

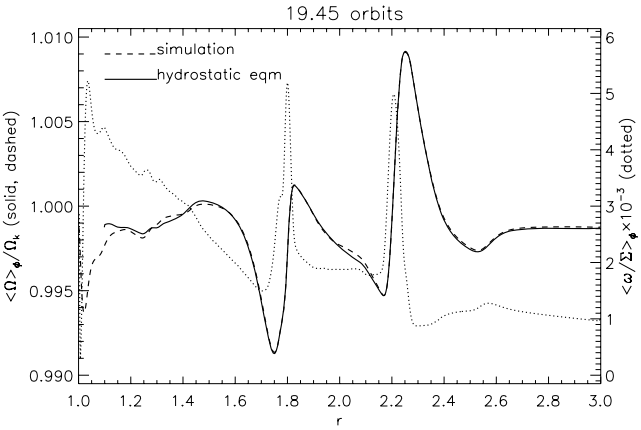

(b) Ω/Ω_k

Figure 8. A comparison of the axisymmetric surface density and angular velocity (scaled by Keplerian speed) profiles obtained by solving equation (18), with the same quantities obtained by azimuthally averaging the simulation data over 2π. The azimuthally averaged vortensity profile from simulation data is also shown (dotted line). The co-orbital region is $r = [1.77, 2.22]$.

equation (18) demonstrates the link between shocks and gap formation. Given the double-ringed vortensity profile $\eta(r)$, which may be estimated by modelling shocks as described above, we can solve equation (18) for the axisymmetric surface density profile $\Sigma(r)$. We will then find that in order for the rings to be in hydrostatic equilibrium a gap in the surface density must be present around the planet's orbital radius, which is in between the vortensity peaks. Sufficiently massive planets induce strong shocks, implying larger vortensity maxima, and hence deeper surface density minima or gaps. Note that the processes described above account for gap formation within the coorbital region as arising from angular momentum transport occurring as material passes through shocks. The shocks associated with high-mass planets in the non-linear regime develop from the wakes associated with Lindblad resonances that occur for small mass planets in the linear regime. Thus, this angular momentum transport can be connected with the Lindblad torques considered in the linear regime.

4.2 Linearized equations

Having established the ring-basic state, we perform linear analysis to determine its stability. Barotropic discs were studied in 3D and 2D by Papaloizou & Pringle (1987) where edges and the roles of the vortensity and outgoing density waves were first considered. The non-barotropic 2D disc case was studied by Li et al. (2000) who assumed that fluid elements moved adiabatically. Our analysis is for a 2D disc with a locally isothermal equation of state as adopted in the simulations. We obtain the governing equation for locally isothermal perturbations by linearizing the continuity equation and the equation of motion as seen in the non-rotating frame in the form

$$\frac{\partial \Sigma}{\partial t} + \nabla \cdot (\Sigma \boldsymbol{u}) = 0 \tag{19}$$

$$\frac{\partial \boldsymbol{u}}{\partial t} + \boldsymbol{u} \cdot \nabla \boldsymbol{u} = -\frac{1}{\Sigma} \nabla P - \nabla \Phi, \tag{20}$$

where $P = c_s^2 \Sigma$ with $c_s^2 = h^2 G M_* / r$. The total potential Φ is assumed fixed. We set

$$\begin{pmatrix} \Sigma \\ u_r \\ u_\phi \end{pmatrix} \rightarrow \begin{pmatrix} \Sigma \\ 0 \\ u_\phi \end{pmatrix} + \begin{pmatrix} \delta\Sigma(r) \\ \delta u_r(r) \\ \delta u_\phi(r) \end{pmatrix} \times \exp \mathrm{i}(\sigma t + m\phi),$$

where the first term on the RHS corresponds to the basic background state, σ is a complex frequency and m, the azimuthal mode number, is a positive integer. The linearized equation of motion (equation 20) gives

$$\delta u_r = -\frac{c_s^2}{\kappa^2 - \bar{\sigma}^2} \left(\mathrm{i}\bar{\sigma} \frac{\mathrm{d}W}{\mathrm{d}r} + \frac{2\mathrm{i}m\Omega W}{r} \right) \tag{21}$$

$$\delta u_\phi = \frac{c_s^2}{\kappa^2 - \bar{\sigma}^2} \left(\Sigma\eta \frac{\mathrm{d}W}{\mathrm{d}r} + \frac{m\bar{\sigma}}{r} W \right), \tag{22}$$

where $W \equiv \delta\Sigma/\Sigma$ is the fractional density perturbation, $\kappa^2 = 2\Omega\Sigma\eta$ is the epicycle frequency expressed in terms of the vortensity η and $\bar{\sigma} \equiv \sigma + m\Omega(r) = \sigma_R + m\Omega(r) + \mathrm{i}\gamma$ is the Doppler-shifted frequency with σ_R and γ being real.

Substituting equations (21)–(22) into the linearized continuity equation

$$\mathrm{i}\bar{\sigma} W = -\frac{1}{r\Sigma} \frac{\mathrm{d}}{\mathrm{d}r} (r\Sigma \delta u_r) - \frac{\mathrm{i}m}{r} \delta u_\phi \tag{23}$$

yields a governing equation for W of the form

$$\frac{\mathrm{d}}{\mathrm{d}r} \left(\frac{\Sigma}{\kappa^2 - \bar{\sigma}^2} \frac{\mathrm{d}W}{\mathrm{d}r} \right) + \left\{ \frac{m}{\bar{\sigma}} \frac{\mathrm{d}}{\mathrm{d}r} \left[\frac{\kappa^2}{r\eta(\kappa^2 - \bar{\sigma}^2)} \right] - \frac{r\Sigma}{GM_* h^2} - \frac{m^2 \Sigma}{r^2(\kappa^2 - \bar{\sigma}^2)} \right\} W = 0. \tag{24}$$

This equation leads to an eigenvalue problem for the complex eigenvalue σ. Corotation resonance occurs at $\bar{\sigma} = 0$ which requires $\gamma = 0$ for it to be on the real axis. Then for the equation to remain regular the gradient of the terms in square brackets must vanish at corotation. This results in the requirement that the gradient of ηr vanishes there. Because the sound speed varies with radius, this is slightly different from the condition that the gradient of η should vanish which applies in the barotropic strictly isothermal case (Papaloizou & Pringle 1984, 1985; Papaloizou & Lin 1989). However, because η varies vary rapidly in the region of interest and the modes we consider are locally confined in radius, this difference is of no essential consequence. Lindblad resonances occur when $\kappa^2 - \bar{\sigma}^2 = 0$, but as is well known and can be seen from formulating a governing equation for δu_r rather than W, these do not result in a singularity.

4.2.1 *Simplification of the governing ODE*

It is useful to simplify equation (24) to gain further insight. To to this, we consider modes localized around the corotation circle such that the condition $\kappa^2 \gg |\bar{\sigma}^2|$ is satisfied. Beyond this region the mode amplitude is presumed to be exponentially small. Now, recognizing that $GM_* h^2/r = c_s^2$, the ratio of the second to last to last term in equation (24) is

$$\frac{r^2\kappa^2}{m^2 c_s^2} \sim \frac{1}{m^2 h^2}.$$

For a thin disc, $h \ll 1$, so if we consider $m = \mathrm{O}(1)$ this ratio is large and the last term in equation (24) can be neglected. This is also motivated by the fact that only low m modes are observed in simulations. Doing this and replacing $\kappa^2 - |\bar{\sigma}^2|$ by κ^2, equation (24) reduces to the simplified form

$$\frac{\mathrm{d}}{\mathrm{d}r} \left(\frac{r c_s^2 \Sigma}{\kappa^2} \frac{\mathrm{d}W}{\mathrm{d}r} \right) + \left\{ \frac{m}{\bar{\sigma}} \frac{\mathrm{d}}{\mathrm{d}r} \left[\frac{c_s^2}{\eta} \right] - r\Sigma \right\} W = 0. \tag{25}$$

We comment that in this form equation (25) is valid for any fixed c_s profile.

4.2.2 *Necessity of extrema*

Multiplying equation (25) by W^* and integrating between $[r_1, r_2]$ assuming, consistent with a sharp exponential decay, that $W = 0$ or $\mathrm{d}W/\mathrm{d}r = 0$ at these boundaries, we find that

$$\int_{r_1}^{r_2} \frac{m}{\bar{\sigma}} \left(\frac{c_s^2}{\eta} \right)' |W|^2 \mathrm{d}r = \int_{r_1}^{r_2} r\Sigma |W|^2 \mathrm{d}r + \int_{r_1}^{r_2} \frac{r\Sigma c_s^2}{\kappa^2} |W'|^2 \mathrm{d}r, \tag{26}$$

where derivatives are indicated with a prime. Since the RHS is real, the imaginary part of the left and side must vanish. For general complex σ, this implies that

$$\gamma \int_{r_1}^{r_2} \frac{m}{(\sigma_R + m\Omega)^2 + \gamma^2} \left(\frac{c_s^2}{\eta} \right)' |W|^2 \mathrm{d}r = 0. \tag{27}$$

Thus, for a growing mode ($\gamma \neq 0$) to exist we need $(c_s^2/\eta)' = 0$ at some r in $[r_1, r_2]$. For our disc, c_s^2 varies on a scale $\mathrm{O}(r)$, but η varies

on a scale $H \ll r$, thus given that the range of relative variation of the vortensity η is of the order of unity we infer that this quantity needs to have stationary points in order for there to be unstable modes. In the barotropic case, Papaloizou & Lin (1989) have shown that vortensity maxima are stable while minima are associated with instabilities. We expect these conclusions to apply here also because of the local nature of the modes of interest. We can approximate $c_s^2 \sim$ constant, or equivalently adopt a barotropic equation of state locally without changing the character of the problem. Referring back to Fig. 8(a), it is clear that our basic state satisfies the necessary criterion for instability.

4.3 Numerical solution of the eigenvalue problem

We have solved the eigenvalue problem for the full equation (24) using a shooting method that employs an adaptive Runge–Kutta integrator and a multidimensional Newton method (Press et al. 1992). For low m (≤ 3), unstable modes mainly comprise an evanescent disturbance near co-rotation (or the vortensity minimum at $r = r_0$) and the simple boundary condition $W = 0$ applied at the inner boundary $r/r_\mathrm{p} = 0.55$ and the outer boundary $r/r_\mathrm{p} = 1.5$ produces good results. As m increases, the Lindblad resonances approach $r = r_0$ and a significant portion of the mode is wave like requiring the application of outgoing radiation boundary conditions. We determined these using the WKBJ approximation (see e.g. Korycansky & Papaloizou 1995).

4.3.1 Eigenmode calculations

We now discuss some example solutions to illustrate the instability of gap edges. We recall that the simulations indicate the ultimate dominance of small m values. One class of mode is associated with the inner vortensity ring while another is associated with the outer ring.

As a typical example of the behaviour that is found for low m, each type of eigenmode for $h = 0.05$ and $m = 3$ is shown in Fig. 9. The background vortensity profile is also shown. The instabilities ($\gamma < 0$) are associated with the vortensity minima at the inner and outer gap edges, as has also been observed by Li et al. (2005) in simulations. The modes are evanescent around corotation and the vortensity peaks behave like a wall through which the instability scarcely penetrates. The mode decays away from $r = r_0$. For $m = 3$, Lindblad resonances occur at $r_L/r_0 = 0.76,\ 1.21$ from which waves travelling away from corotation are emitted. However, the oscillatory amplitude is at most $\simeq$20 per cent of that at $r = r_0$. Hence, for low-m the dominant effect of the instability will be due to perturbations near co-rotation. Increasing m brings r_L even closer to r_0, waves then propagate through the gap. The growth time-scale of the inner mode with $m = 3$ is $\sim 14 P_0$. The outer mode has a growth rate that is about three times faster. Very similar results and growth rates were found for $m = 1$ and 2. Since the instability grows on dynamical time-scales, we expect non-linear interaction of vortices to occur within few tens of orbits and to affect planet migration if the latter were also on similar or longer time-scales.

After the onset of linear instability and the formation of several vortices, it has been observed that non-linear effects cause them to eventually merge into a single vortex (de Val-Borro et al. 2007). This eventually interacts with the planet. In the fiducial simulation, rapid migration begins at $55 P_0$ which is compatible with the characteristic growth times found from linear theory.

Fig. 9 indicates that the outer edge is more unstable than inner edge. The vortensity peaks are of similar height, but the inner minimum in η is less pronounced than outer because of the background profile. In this sense, the outer edge profile is more extreme, and hence less stable.

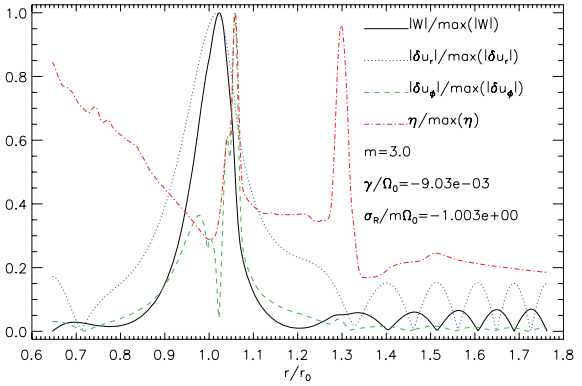

(a) Inner edge

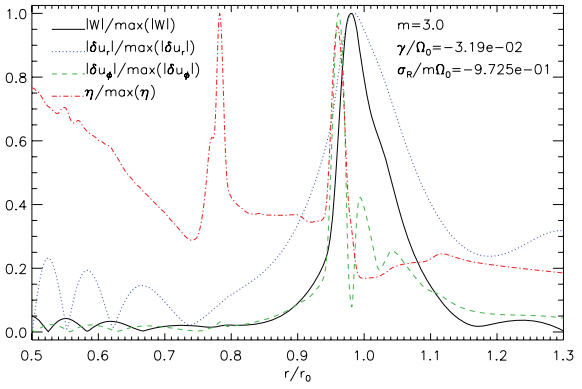

(b) Outer edge

Figure 9. $m = 3$ eigenmodes obtained with the boundary condition $W = 0$. The perturbed quantities are plotted as $|W|$ (solid line, black), $|\delta u_r|$ (dotted line, blue), $|\delta u_\phi|$ (dashed line, green) each scaled by their maximum values as functions of r for the interval [1.1, 3.0]. The background vortensity profile is also shown (dash–dotted line, red). The inner and outer vortensity minima correspond to $r_0 = 1.7$ and 2.3, respectively.

For illustration, we show in Fig. 10 eigenfunctions for the $m = 7$ mode of the outer ring. The equivalent mode was not found for the inner edge because high m are quenched. Radiative boundary conditions were adopted in this case. Although the WKBJ condition is the appropriate physical boundary condition, its application here is uncertain because the boundaries cannot be considered 'far' from the gap. However, solutions are actually not sensitive to boundary conditions as reported by de Val-Borro et al. (2007). Note the two spikes in δu_r and δu_ϕ at $r/r_0 \simeq 0.90,\ 1.09$ which correspond to Lindblad resonances. These are not singularities as can be seen from $W(r)$ which is smooth there; other eigenfunctions were calculated from the numerical solution for W and thus may be subject to numerical errors. We see that increasing m increases the amplitude in the wave-like regions of the mode, but the growth rate is smaller than for $m = 3$. As the instability operates on dynamical time-scales, low-m modes will dominate over high-m modes, particularly through non-linear evolution and interaction of the former.

We have also examined solutions with $h = 0.03,\ 0.04$ and 0.06. In general, as h is lowered, γ becomes more negative. As the disc temperature is lowered with h, there are stronger shocks, and larger modifications to the disc profile, or steeper gradients. Hence, we

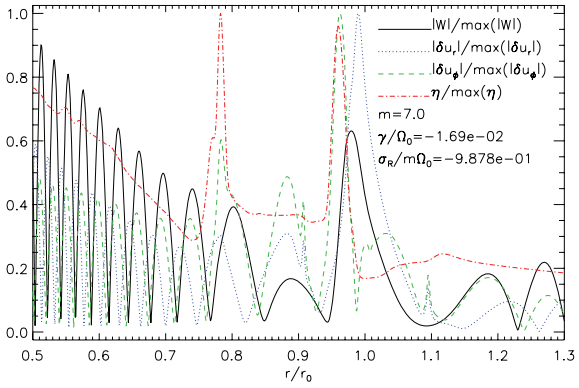

Figure 10. $m = 7$ eigenmodes associated with the outer edge, obtained with WKBJ boundary condition. The perturbed quantities $|W|$ (solid line, black), $|\delta u_r|$ (dotted line, blue), $|\delta u_\phi|$ (dashed line, green) each scaled by their maximum values are plotted as functions of r for the interval [1.1, 3.0]. The background vortensity profile is also shown (dash–dotted line, red). The radius of the outer vortensity minima is $r_0 = 2.3$.

expect edges to become more unstable. In the case of $h = 0.03$, the rings become unstable (vortices form) before they reach an approximately axisymmetric state.

Having understood the origin of vortices, we proceed to study their effect on planet migration, in the type III regime.

5 SIMULATIONS OF FAST MIGRATION DRIVEN BY VORTEX–PLANET INTERACTION

We now present hydrodynamic simulations of disc–planet interactions where the planet is free to migrate, so that $r_\mathrm{p} = r_\mathrm{p}(t)$. Vortices that form in the co-orbital region near the gap edge move through the co-orbital region and cause torques to be exerted on the planet. The interaction between such large-scale structures and the planet leads to non-monotonic type III migration and is the focus of this section. The type III torque increases with the co-orbital mass deficit δm:

$$\delta m = 8\pi r_\mathrm{p} B_\mathrm{p} \left[x_s w(-x_s) - \int_{-x_s}^{0} w(x)\mathrm{d}x \right] \tag{28}$$

(Masset & Papaloizou 2003), where $w = \Sigma/\omega$ and $B_\mathrm{p} = \frac{1}{2r}\partial_r(r^2\Omega)$ is the Oort constant evaluated at the planet radius r_p. Hence, the inverse vortensity Σ/ω will be central to the discussion.

The simulations described below have computational domain $r = [\,0.4, 4.0\,]$ with resolution $N_r \times N_\phi = 768 \times 2304$. The planet is set in circular orbit after which the initial radial velocity is set to be $v_r = -3\nu/2r$, as expected for a steady accretion disc (Lynden-Bell & Pringle 1974). The initial surface density is chosen to be $\Sigma_0 = 7.0$, corresponding to a few times the value appropriate to the minimum-mass solar nebula in order to achieve rapid migration when a typical viscosity $\nu_0 = 1$ is used (Masset & Papaloizou 2003; de Val-Borro et al. 2007). For most of these simulations the full planet potential is applied from $t = 0$. Similar results were obtained if the potential is switched on over 5 orbits as in Section 3 where the formation of vortensity rings was discussed. In those cases, vortices were observed to form. Switching on the planet potential over several orbits does not weaken the instability, vortensity rings build up and vortex–planet interactions still occur (see below), although at a slightly later time than if the planet is introduced at $t = 0$.

Type III migration is numerically challenging due to its dependence on flow near the planet, one issue being the numerical resolution. D'Angelo, Bate & Lubow (2005) reported the suppression of type III migration in high-resolution simulations. The main migration feature discussed below is brief phases of rapid migration due to vortex–planet interaction, which does not depend on conditions very close to the planet. Our preliminary experiments with resolutions of $N_r \times N_\phi = 192 \times 576$, 256×768 both show such behaviour; thus, we believe the higher resolution used below is sufficient to study this interaction.

The locally isothermal equation of state implies no temperature changes due to the planet. This could lead to mass accumulation in the Hill sphere and thus spurious torques from within. Pepliński et al. (2008a) used an equation of state where temperature increases close to the planet. We have also considered this model where the modification is applied to within the Hill sphere and at $t = 0$, $c_s(r = r_\mathrm{p})$ is 18 per cent higher than the local isothermal value. This again yields vortex–planet scattering, which is an indication that significant torque contribution during the interaction is not due to material inside the Hill sphere. Qualitatively, the same phenomenon is observed for the case where the temperature increase is 38 per cent.

Finally, there is the issue of softening. We set $\epsilon = 0.6H$ as before, but have considered softenings of $0.5H$ and $0.7H$ and both cases display vortex–planet interaction, although at earlier times when ϵ is lower. This is expected since smaller softening has the same effect as increasing the planet mass, and thus producing a more unstable disc.

5.1 Viscosity and vortices

We have shown above that the ring structures formed by a Saturn-mass planet in our case are linearly unstable. It has been shown through numerical simulations that such instabilities are expected to lead to vortex production (Li et al. 2001) and this has been seen when steep surface density gradients are present outside the co-orbital region of a lower mass planet (Koller et al. 2003; Li et al. 2005). Non-monotonic migration was observed by Ou et al. (2007) when a vortex is present inside the co-orbital region, but the role of the vortex was not analysed in detail.

Fixed orbit simulations of disc–planet interactions show that a dimensionless viscosity of the order of 10^{-5} suppresses vortex formation (de Val-Borro et al. 2007). As a consequence, studies using viscous discs typically yield smooth migration curves. We have confirmed this in our case with numerical simulations.

5.2 Dependence of the migration rate on viscosity

We first study type III migration as a function of viscosity. The effect of vortices appears at low viscosities. Fig. 11 shows the orbital semimajor axis $a(t)$ for viscosities $\nu_0 = 0$–1. As the orbit is very nearly circular, $a(t)$ is always close to the instantaneous orbital radius $r_\mathrm{p}(t)$. In order to estimate the residual numerical viscosity, we reduced the value of ν_0. We found that only for ν_0 below $\sim 10^{-3}$ were almost identical $a(t)$ curves to that obtained with $\nu_0 = 0$ produced. This suggests that the numerical viscosity is of the order of $\nu = \mathrm{O}(10^{-8})$ which is much smaller than the typically adopted physical viscosity of $\nu = 10^{-5}$. We remark that this estimate of the magnitude of the numerical viscosity is in line with that made by de Val-Borro et al. (2007) for the non-Cartesian grid based codes they used.

With the standard viscosity $\nu_0 = 1$, $a \to a/2$ in less than $100P_0$, implying type III migration (Papaloizou et al. 2007). Comparing different ν_0, $a(t)$ is indistinguishable for $0 < t \lesssim 15$, since viscous

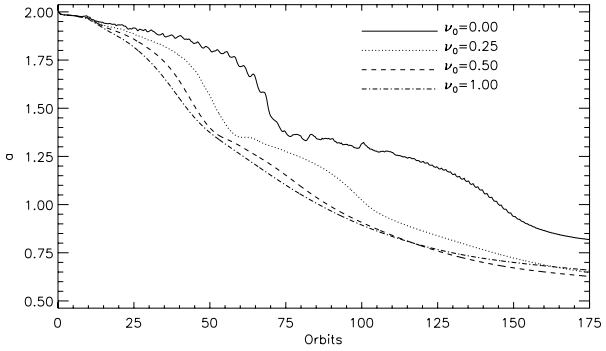

Figure 11. Type III migration as a function of viscosity.

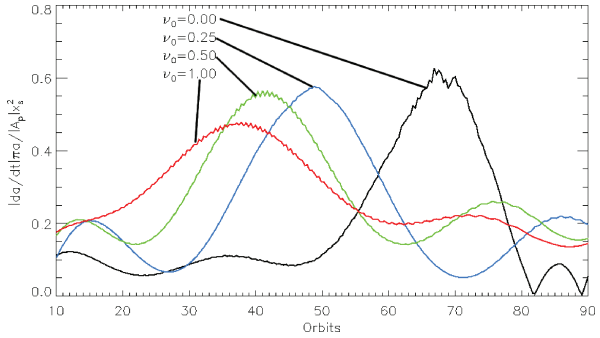

Figure 12. Evolution of χ, the ratio of libration-to-migration time-scale as a function of viscosity. Libration time is measured at $r_\mathrm{p} - r = x_s$ and migration time-scale is that across x_s.

time-scales are much longer than the orbital time-scale. At $t = 20$, $|\dot{a}|$ increases with ν_0. In the limit $\nu \to 0$, the horseshoe drag for a fixed orbit is $\propto \nu$ (Balmforth et al. 2001; Masset 2002). However, in this case $\dot{a} \neq 0$ there is a much larger rate-dependent torque responsible for type III migration, for which explicit dependence on viscosity has not been demonstrated analytically.

Migration initially accelerates inwards ($\dot{a}$, $\ddot{a} < 0$) and subsequently slows down at $r \sim 1.4$ (independent of ν_0). For $\nu_0 = 1.0$, 0.5, migration proceeds smoothly, decelerating towards the end of the simulation at which point the orbital radius has decreased by a factor of ∼2.7. Migration curves for $\nu_0 = 1.0$ and 0.5 are quantitatively similar. Lowering ν_0 further enhances the deceleration at $r \sim 1.4$ until in the inviscid limit the migration stalls before eventually restarting.

Despite differences in detail, the overall extent of the orbital decay in all of these cases is similar. This is expected in the model of type III migration where the torque is due to circulating fluid material switching from $r_\mathrm{p} - x_s$ to $r_\mathrm{p} + x_s$. In this model, the extent of the orbital decay should not depend on the nature of the flow across r_p, but only on the amount of disc material participating in the interaction, or equivalently the disc mass and this does not depend on ν. On the other hand, the flow may not be a smooth function of time with migration proceeding through a series of fast and slow episodes as observed in Fig. 11. Our argument is only valid if migration proceeds via the type III mechanism. We have not explored viscosities, ν, exceeding a few times 10^{-5} in detail but migration time-scales seen in test cases indicate that type III migration then ceases to operate.

5.3 Stalling of type III migration

The issue discussed here is what inhibits the growth of $|\dot{a}|$? Descriptions of (inward) type III migration usually assume that the libration time at $r_\mathrm{p} - x_s$ is much less than the time to migrate across the co-orbital region (Masset & Papaloizou 2003). This implies that

$$\chi \equiv \frac{|\dot{a}|\pi a}{|A_\mathrm{p}|x_s^2} \ll 1, \tag{29}$$

where $A_\mathrm{p} = 1/2(\partial\Omega/\partial r)$ at $r_\mathrm{p}(t)$ and a is the changing semimajor axis. Papaloizou et al. (2007) present a similar critical rate, but with the same dependence on Ω, a, x_s. If equation (29) holds, co-orbital material is trapped in libration on horseshoe orbits and migrates with the planet. When $\chi \gtrsim 1$, the horseshoe region shrinks to a tadpole, and material is trapped in libration about the L4 and L5 Lagrange points (as observed by Pepliński et al. 2008b). This can tend to remove the co-orbital mass deficit δm[1] which reduces the migration torque. Comparing χ for cases shown in Fig. 12, it is clear that migration with $\chi \ll 1$ (hereafter in this context termed as slow migration even though it may be much faster than type II migration) does not always hold, with $\max(\chi) \sim 0.6$ being comparable for different ν_0. By following the evolution of a passive scalar, we checked that horseshoe material no longer migrates with the planet when $|\dot{a}|$ is large. This occurs for all ν but only the low-viscosity cases exhibit stalling. Hence, while horseshoe material is lost due to fast migration, this is not responsible for stopping it.[2] By examining the inviscid case in detail later, we show that the stopping of migration is due to the flow of a vortex across the co-orbital region, where some of it becomes trapped in libration.

5.4 The connection between the vortensity and fast migration

The difference between the value of the inverse of the vortensity Σ/ω evaluated in the co-orbital region and the value associated with material that passes from one side of the co-orbital region to the other defines the co-orbital mass deficit δm in Masset & Papaloizou (2003). It is often assumed that the vorticity is slowly varying so that the difference in the values of inverse vortensity reduces, to within a scaling factor, simply to the difference in the values of the surface density.

Although Masset & Papaloizou (2003) assumed steady, slow migration in the low-viscosity limit, it is nevertheless useful to examine its evolution in relation to the migration of the planet (Fig. 11). Fig. 13 shows the azimuthally averaged Σ/ω-perturbation following planet migration. Introducing the planet modifies the co-orbital structure on orbital time-scales. Vortensity rings develop at $r - r_\mathrm{p} \simeq \pm 2r_\mathrm{h}$ for $t \lesssim 10$ (Fig. 13a). We showed above that this initial modification is due to spiral shocks extending into the horseshoe region and also that the ring-structure is unstable to the production of vortices.

Increasing ν reduces the rings' amplitude, but their locations are unaffected. Taking the length-scale of interest as $l = r_\mathrm{h} \simeq 0.1$, for $\nu_0 = 1$ the viscous time-scale is $t_d = l^2/\nu \simeq 56P_0$. Hence, at $t \lesssim 10$ viscous diffusion is not significant even locally. Thus, ring formation is not sensitive to the value of ν. We note the correspondence between the similarity of the Σ/ω profiles and similarity in $a(t)$ for

[1]We can regard the process of changing from a partial gap extending for nearly the whole azimuth to one with a smaller azimuthal extent, as gap filling.

[2]One may intuitively expect migration to be self-limited.

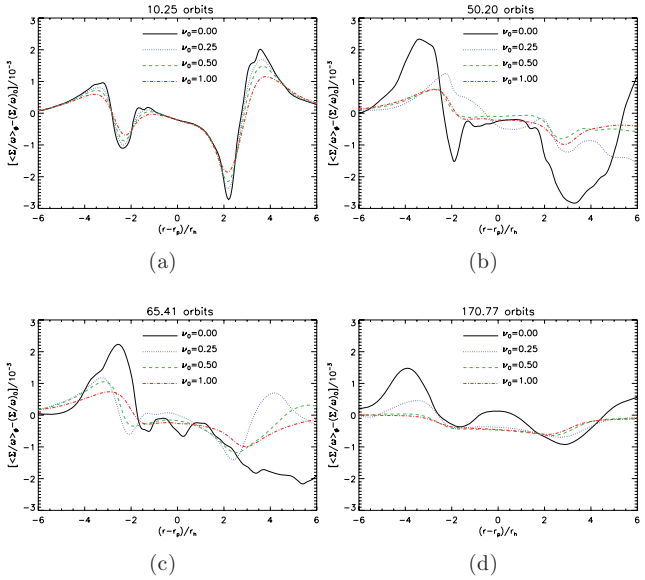

Figure 13. Σ/ω-perturbation for different viscosities for the case $\Sigma_0 = 7$ and $M_p = 2.8 \times 10^{-4}$. Here, we use $\omega = r^{-1}\partial_r(ru_\phi)$ to approximate the vorticity. This is valid since $|u_r| \ll |u_\phi|$.

different ν in the initial phase. That is, the co-orbital disc structure determines migration (Masset & Papaloizou 2003). Dependence on the value of the viscosity is seen beyond $t = 50$ (Fig. 13b), producing much smoother (and similar) profiles for $\nu_0 = 0.5$ and $\nu = 1.0$.

For a fixed orbit, we would expect profiles to be smoothed on a viscous time-scale. When there is migration, we should also consider advection of vortensity (in the planet frame). Following the planet, the perturbed profile can be smooth if the planet migrates through the background without carrying its original co-orbital material. This can be regarded as the loss of horseshoe material due to fast migration. Any deviation from the background must then be due to local vortensity generation/destruction as the planet moves through (e.g. shocks).

In Fig. 13(b), only the inviscid case is still in slow migration, and only this disc retains the inner ring (low Σ/ω). This suggests that the inner vortensity ring inhibits inward migration. In terms of δm, for $\nu \neq 0$ the planet resides in a gap (co-orbital Σ/ω is less than that at the inner separatrix, or $\delta m > 0$) whereas in the inviscid case $\delta m \sim 0$.

Consider the $\nu = 0$ case. The outer vortensity ring has widened to $\sim 2r_h$ (cf. Fig. 13a). It is centred at $3r_h$ so that co-orbital dynamics may not account for it. However, the migration implies a flow of material across r_p from the interior region. The increased region of low Σ/ω exterior to the planet may be due to this flow. Note the high-Σ/ω ring at $+4r_h$ in Fig. 13(a) is no longer present in Fig. 13(b) because this ring is not co-orbital and therefore does not migrate with the planet.

At $t = 65$ (Fig. 13c), the $\nu_0 = 0.5$ and $\nu = 1.0$ cases continue smooth rapid migration (Fig. 11) with qualitatively unchanged profiles. For $\nu_0 = 0.25$, characteristic vortensity double rings redevelop after a stalling event at $t \sim 60$ (Fig. 11). The peaks and troughs of Σ/ω recover forms that are close to those in the initial phase (Fig. 13a). At this time, the inviscid case is in rapid migration.

Fig. 13(d) shows the final Σ/ω-perturbation profiles. Viscous cases are in slow migration, and have much smoother profiles. This can be due to diffusion (since we are at late stage of evolution) and/or migration across the background, in both situations there is little disc material carried by the planet. The inviscid case is also in slow migration but retains the double-ring structure. This indicates two possible co-orbital configurations which slow down type III migration.

In this section, we reviewed the disc vortensity evolution and its connection to the state of migration. A correlation between migration (fast, slow) and co-orbital structure is apparent. The effective action of viscosity appears to be through its modification of the disc structure, rather than associated viscous torques acting on the co-orbital region.

5.5 Evolution of the co-orbital region

In Fig. 14, we illustrate the evolution of the following quantities associated with the co-orbital region that are related to the migration torque induced on the planet.

(i) The gravitational torque acting on the planet due to fluid with $|r - r_p| \leq 2.5r_h$, excluding fluid within r_h of the planet. This includes co-orbital material and orbit-crossing fluid, the latter being responsible for the type III torque.

(ii) The co-orbital mass deficit δm is computed from azimuthally averaged, 1D disc profiles. We took the separatrices to be at $|r - r_p| = 2.5r_h$.

(iii) M_{tr}, the mass of a passive scalar initially placed such that $|r - r_p| = 2r_h$.[3] Note that M_{tr} = constant if it migrates with the planet.

(iv) The average density $\langle\Sigma\rangle$ and vortensity $\langle\omega/\Sigma\rangle$ of the region $|r - r_p| < 2.5r_h$.

The evolution of viscous and inviscid cases is qualitatively similar up to the stalling indicated by vertical lines in Fig. 14. Prior to this, there is a rapid migration phase associated with large a negative torque which we find originates from material crossing the planet orbit. Co-orbital torques are oscillatory and the period/amplitude is longer/larger for $\nu_0 = 0$ than for $\nu_0 = 0.5$. During rapid migration phases, the inviscid torque is twice as negative than in the viscous case. While the torque in a viscous disc remains negative, torques in an inviscid disc can be positive due to the formation of large-scale vortices. Note that the torque does not originate from within the Hill sphere since it is excluded from the summation.

Migration is slow until sufficient difference builds up between co-orbital and circulating flow at which point there is a sudden flow-through the co-orbital region. At the same time, there is significant loss of the original horseshoe material (M_{tr} decreases by $\sim$80 per cent). The flow-through is reflected in $\nu_0 = 0.5$ ($\nu_0 = 0$) by a $\sim$ 17 per cent (36 per cent) increase in $\langle\Sigma\rangle$ from $t = 25$ to 50 ($t = 50$–75). In the case of zero viscosity, this material is in the form of a high-surface-density vortex. We note from Fig. 14(b) that there is a repeated episode where there is a fall followed by a rise in $\langle\Sigma\rangle$. However, in the late stages of evolution of the case with $\nu_0 = 0.5$, $\langle\Sigma\rangle$ decreases monotonically and the migration is slower.

The co-orbital mass deficit is initially negative[4] as the rings develop. It subsequently increases resulting in the onset of type III

[3] Due to the uncertainty in the horseshoe half-width x_s we put the tracer well within the region defined by $x_s = 2.5r_h$ to ensure it is co-orbital.

[4] Ring structure in the vicinity of the separatrix means that the sign of δm is sensitive to the adopted value of x_s. Here, we regard δm as a representation of gap depth, so we fix $x_s = 2.5r_h$.

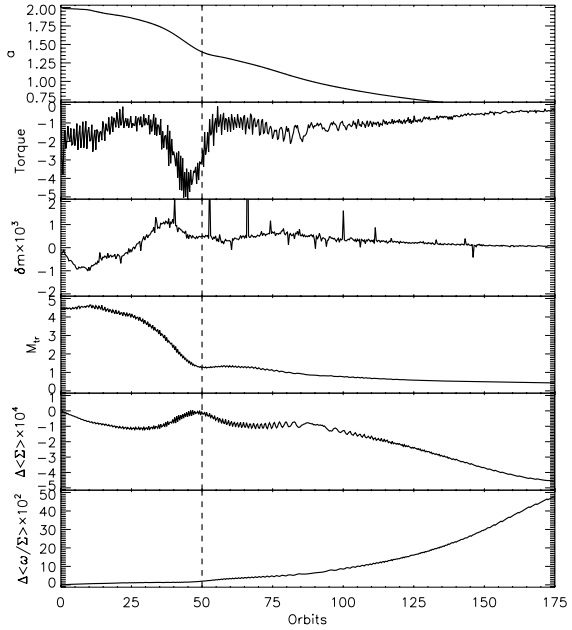

(a) $\nu_0 = 0.5$

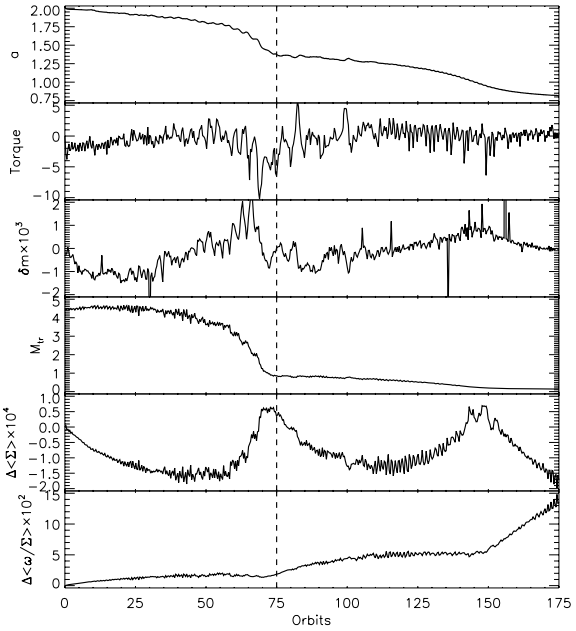

(b) $\nu_0 = 0$

Figure 14. Effect of viscosity on co-orbital evolution. The time evolution is illustrated for the model with $\nu = 0.5$ (upper panel) and for the inviscid model (lower panel). From top to bottom of each panel the evolution of the orbital radius, $a(t)$, the co-orbital mass deficit δm, the torque, the tracer mass $M_{\rm tr}$, the surface density $\langle\Sigma\rangle$ and the vortensity $\langle\frac{\omega}{\Sigma}\rangle$ are plotted. Angle brackets denote space averaging over the annulus $[r_{\rm p} - 2.5r_{\rm h}, r_{\rm p} + 2.5r_{\rm h}]$ and Δ denotes perturbation relative to $t = 0$. The vertical line indicates stalling of migration.

migration and is most positive during the following rapid migration phase, with peak values $\delta m \times 10^3 \sim 1$, 2 for $\nu_0 = 0.5$, 0, respectively. $\delta m \times 10^3$ then falls to $+0.5$ in the viscous case but to $\lesssim 0$ in the inviscid case. In the latter case, material flowing into the co-orbital region removes the co-orbital mass deficit and type III is suppressed; migration experiences a more abrupt stall. δm increases again for $\nu_0 = 0$ while it remains approximately constant for $\nu_0 = 0.5$ and decreases towards the end. Type III migration can restart in the inviscid disc but such behaviour is not observed for large viscosity. Type III is not operating in the late stages of the viscous case, in contrast to the inviscid evolution where fast type III migration is recurrent, faster than in the cases with applied viscosity, and is associated with large values of δm.

The above discussion shows that the magnitude of the applied viscosity is significant in determining the character of the migration. This is because the form of the flow through the co-orbital region is sensitive to the choice of viscosity. In particular, for high viscosity, this flow is smooth and there is less disruption of the co-orbital region.

6 VORTEX–PLANET INTERACTION

We now focus on the inviscid case where the role of vortices significantly affects the migration. We consider three phases apparent from Fig. 11. These are: (a) $t \lesssim 45$ (slow migration); (b) $60 \lesssim t \lesssim 70$ (rapid migration); (c) $t \sim 75$ (stalling) and (d) $75 \lesssim t \lesssim 110$ (second phase of slow migration). Typical migration rates at various times are $\dot{a}(25) \sim -3\times10^{-3}$; $\dot{a}(65) \sim -2\times10^{-2}$ and $\dot{a}(85) \sim -2\times10^{-3}$. The vortex-induced rapid migration (phase b) is almost an order of magnitude faster than the phases (a) and (d). Hence, we refer to the latter as slow migration, but more accurately they are migration associated with gap formation. They are not necessarily slow in comparison to type I or type II migration.

Different migration phases correspond to different disc structures. Fig. 15 shows the global surface density evolution. At $t = 24.75$, during the slow migration phase (a), the planet resides in a partial gap ($r \simeq r_{\rm p} \pm 2.3r_{\rm h}$) with surface density ∼20 per cent lower than Σ_0. The gap is circular but non-axisymmetric with a low surface density arc along the outer gap edge trailing the planet. A partial gap is necessary for the Type III migration mode (Papaloizou & Terquem 2006) but not sufficient. A surface density asymmetry ahead/behind the planet is needed to provide the net co-orbital torque (Artymowicz 2004a). At this stage, this is too weak. Further azimuthal density asymmetry has developed in the gap by $t = 55$ and there is a factor of ~ 3 variation in the gap surface density, but the asymmetry is still limited.

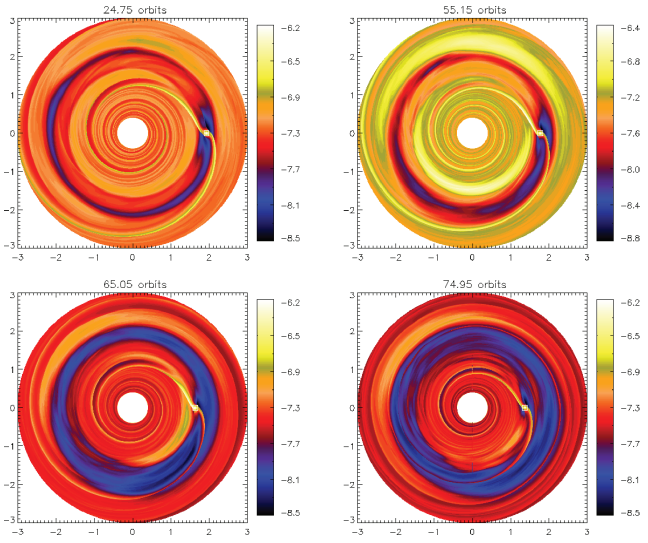

Figure 15. The evolution of ln Σ from early slow migration to stalling (∼75 orbits).

Strong asymmetry can be provided by large-scale vortices near the gap edges of azimuthal extent $\Delta\phi \sim \pi$ (Fig. 15). The outer (inner) vortex rotates clockwise (counterclockwise) relative to the planet so they are not co-orbital. Their origin was explained as a natural consequence of the instability of the vortensity rings (see Section 4), their occurrence near gap edges has a strong influence on the type III migration mode.

At $t = 65.05$, Fig. 15 shows that the planet is just inside the inner gap edge. The surface density contrast in the neighbourhood of the planet is largest as the inner vortex enters the co-orbital region from behind the planet. It exerts a net negative torque as the material crosses the planet orbit and enters (is scattered into) the exterior disc, and this snapshot corresponds to fast migration (phase b). At $t = 75$, the migration stalls and the planet no longer resides inside a gap. The planet has effectively left its gap by scattering vortex material outwards. This completes a single vortex–planet episode, during which the outer vortex simply circulates around the original outer gap edge and does not influence the co-orbital dynamics, though it contributes an oscillatory torque on the planet.

The vortex–planet interaction is magnified in Fig. 16. At $t = 65$, the vortex circulates at $\sim r_p - 3r_h$ and has radial extent $\sim 3r_h$. The gap depth is largest and the migration is fast. As the planet migrates inwards, the vortex splits with some material entering the co-orbital region while the rest continues to circulate ($t = 70$). Vortex material becomes trapped just behind the planet at $t = 75$, which would suggest a negative torque. However, the surface density distribution does not support the usual type III migration where horseshoe material moves with planet. Furthermore, the planet no longer resides in a gap. Part of the original horseshoe material is replaced with vortex material and gap filling takes place. The co-orbital mass deficit is lost and the migration stalls.

It is useful to examine the evolution of Σ/ω, or inverse vortensity, since it defines co-orbital mass deficit δm that drives the type III torque (Masset & Papaloizou 2003). This is illustrated in Fig. 17. In inviscid discs, Σ/ω is approximately conserved following a fluid so we can track material. The vortensity ring basic state and its stability were discussed in Section 4 (see Fig. 7). By $t = 55$, the inner vortex has formed via non-linear evolution of the instability and begins to interact with co-orbital region. Vortensity conservation implies that

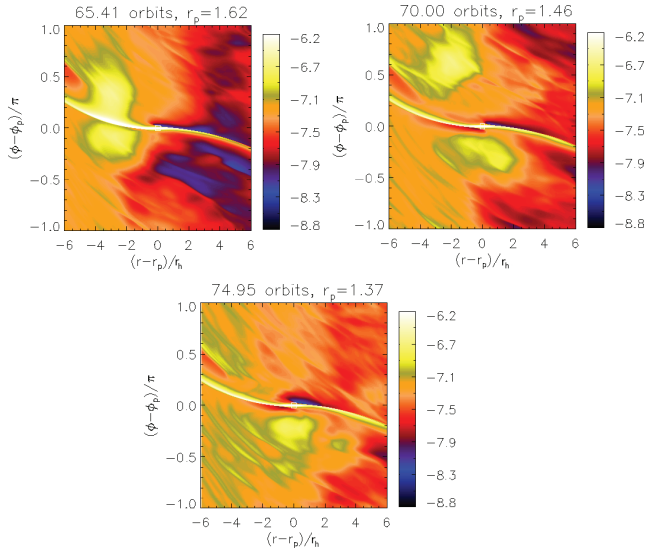

Figure 16. Illustration of the surface density evolution from the start of rapid migration to stalling at $t = 75$. Maps of ln Σ are plotted.

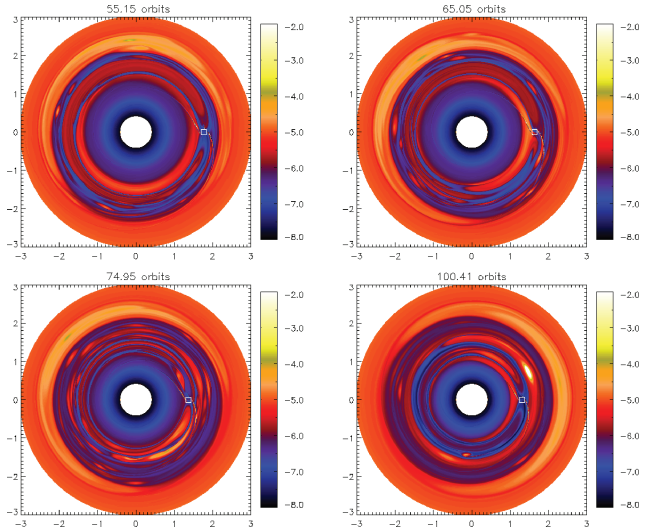

Figure 17. Vortensity evolution: maps of the inverse vortensity $\ln(\Sigma/\omega)$ are plotted spanning the time interval from early slow migration to stalling (∼75 orbits) to the second phase of slow migration.

the 'red blobs' near the outer ring were part of the inner vortex, consistent with inward migration of the planet via Type III (see Fig. 17). Each time this vortex passes by the planet, some of its material crosses the planet orbit from behind, thereby exerting a negative torque. Rapid migration at $t = 65$ occurs when the main vortex body flows across the co-orbital region. The inner ring is disrupted and no longer extends 2π in azimuth.

This contrasts with the usual type III scenario where material simply transfers from inner to outer disc leaving the co-orbital region unaffected. In the inviscid disc, disruption is *necessary* due to the existence of vortensity rings of much higher vortensity than the vortex. Under type III and vortensity conservation, vortex material must cross the planet orbit without changing its vortensity. This would not be possible if a ring structure is maintained. In this sense, the vortensity rings oppose the type III mode. Hence, migration is slow until significant ring disruption occurs that is associated with the vortex flowing across.

When migration stalls at $t = 75$, Fig. 17 shows that the vortensity rings are much less pronounced compared to initial phase. The vortex splits into several smaller patches circulating in the original gap. At the planet's new radius, material of high Σ/ω fills the new co-orbital region, corresponding to lower co-orbital mass deficit. However, by $t = 85$ (not shown) new vortensity rings are setup near the new orbital radius and are qualitatively similar to those present in the ring basic state. The vortex material which passed to the outer disc during the first rapid migration phase is now irrelevant, much like the outermost vortex. During the buildup to the second rapid migration phase at $t = 100$, there is a single vortex associated with inner gap edge and two associated with the outer ring. This simply leads to a repeat of the first rapid migration phase. However, the presence of a vortex inside the co-orbital region, from the first rapid migration phase reduces the co-orbital mass deficit (Fig. 14b) and hence the migration rate for the second rapid phase (at $t \sim 140$).

6.1 The effect of changing the disc mass

Here, we consider type III migration in inviscid discs of different masses obtained by scaling the parameter (Σ_0). Simulations here had a resolution $N_r \times N_\phi = 512 \times 1536$.

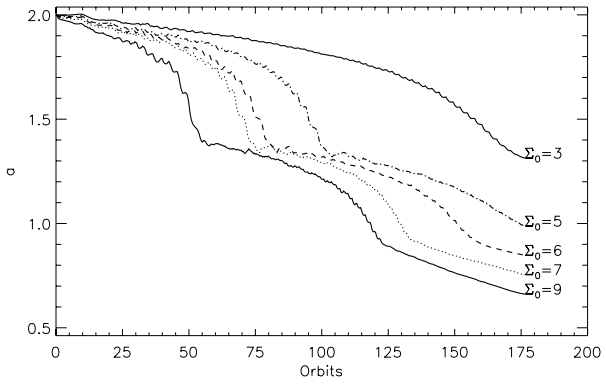

Figure 18. Vortex-induced migration in discs with different scalings of the initial surface density profile. The extent of rapid migration is independent of the initial surface density scaling.

Fig. 18 shows migration as a function of Σ_0. For $\Sigma_0 = 5$–9, the planet migrates by the same amount during the first rapid migration phase and stalls at the same radius. This is also observed for a second rapid migration phase for $\Sigma_0 = 6$–9. Although the highest density case is unphysical due to the lack of inclusion of SG, results are consistent with the notion that rapid migration is initiated by sufficient contrast between co-orbital (gap) and circulating fluid (vortex), measured by δm.

The jump in orbital radius, should it occur, is independent of Σ_0. As the interaction involves the vortex flowing from the gap edge across the co-orbital region, its change in specific angular momentum is independent of density, because the co-orbital region size is fixed by planet mass. The results then suggest the vortex needs to grow to a mass M_v, only dependent on the planet mass, in order to scatter the planet. Since the vortex forms at the gap edge, M_v can be linked to δm because the co-orbital mass deficit depends on the edge surface density.

As the vortex originates from instabilities with growth rate independent of Σ_0, increasing Σ_0 means less time is needed for the vortex to build up to critical mass or density. Hence, increasing surface density only shortens the 'waiting time' before rapid migration. However, if the density is too low, e.g. $\Sigma_0 = 3$, then vortex-induced rapid migration may never occur.

Consider an inner vortex of mass M_v formed by instability at $r_v = r_\mathrm{p} - \beta r_\mathrm{h}$ ($\beta > 0$) with width αr_h, where the Hill radius $r_\mathrm{h} = f_0 r_\mathrm{p}$, $f_0 \equiv [M_\mathrm{p}/(3M_*)]^{1/3}$. M_v is clearly limited by the amount of material that can be gather into the vortex, so that $M_v < 2\pi\alpha r_\mathrm{h} r_v \Sigma$. Taking $M_v/M_\mathrm{p} = 3.5$ as critical for rapid migration[5], this means

$$\Sigma_0 > \frac{3.5 M_\mathrm{p}}{2\pi\alpha f_0(1-\beta f_0) r_\mathrm{p}^2} \times 10^4. \quad (30)$$

Taking representative values found in simulations of $\alpha = 3$, $\beta = 4$ and $r_\mathrm{p} \sim 2$ gives $\Sigma_0 > 3.5$. For such cases rapid, vortex-induced migration was indeed observed (Fig. 18) but for $\Sigma_0 = 3$ it was not. This is similar to the usual requirement that in order for Type III migration to occur for intermediate planets the disc should be sufficiently massive (Masset & Papaloizou 2003). In our case, the limitation is specifically due to the maximum possible vortex mass.

[5]We estimate the vortex mass by monitoring the decrease in total mass of an annulus interior to the inner gap edge.

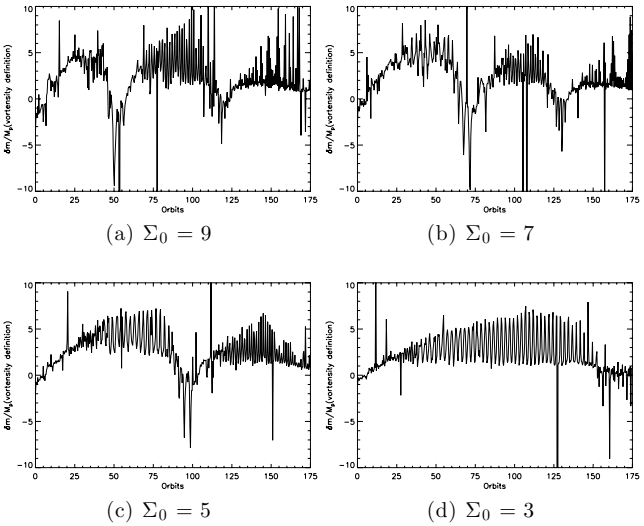

Figure 19. Evolution of the co-orbital mass deficit as defined by inverse vortensity. The average Σ/ω for co-orbital material is taken over $r - r_\mathrm{p} = [-2.5r_\mathrm{h}, 0]$, $\phi = [\phi_\mathrm{p}, \phi_\mathrm{p} - \pi/4]$; and that of circulating material is taken over $r - r_\mathrm{p} = [-6, -2.5]r_\mathrm{h}$, $\phi = [\phi_\mathrm{p}, \phi_\mathrm{p} - \pi/4]$. Very similar behaviour was obtained when we compared the co-orbital and circulating surface densities.

6.1.1 Critical co-orbital mass deficit

In order to link type III migration and vortex–planet scattering, we measured the co-orbital mass deficit δm, which amounts to comparing average inverse vortensity of co-orbital fluid just behind the planet to that of circulating fluid just inside the inner separatrix but also behind the planet:

$$\delta m = 2\pi x_s r_\mathrm{p}^{-1/2}(\langle\Sigma/\omega\rangle_\mathrm{circ} - \langle\Sigma/\omega\rangle_\mathrm{coorb}).$$

This is a simplified version of the definition in Masset & Papaloizou (2003). Results are shown in Fig. 19. The oscillatory nature of δm reflects a vortex circulating at the gap edge, δm maximizing when the vortex is within the patch of fluid where averaging is done. As it grows, the high-vortensity vortex contributes to $\langle\Sigma/\omega\rangle_\mathrm{circ}$ hence favouring type III migration. Cases with rapid migration share the same evolution of δm. δm increases up to ∼4–5 before the vortex first induces fast migration. For $\Sigma_0 = 3$, which does not show such a rapid migration phase, typically $\delta m \lesssim 5$ with smaller amplitude variation.

During fast migration δm rapidly decreases and migration stalls when $\delta m \lesssim 0$. This is because as the vortex flows across the co-orbital radius, it contributes to $\langle\Sigma/\omega\rangle_\mathrm{coorb}$, lowering δm. However, we comment that details depend on the unperturbed ($t = 0$) surface density profile. Discs discussed here initially have uniform surface density. If a surface density $\Sigma \propto r^{-p}$, $p > 0$ were adopted, the planet can be scattered to a region of higher background Σ/ω compared to the flat case, so $\langle\Sigma/\omega\rangle_\mathrm{circ}$ may increase due to the background. We have run simulations with $p = 0.3$, 0.5 and found that the periods of stalling are of shorter duration, consistent with the discussion above regarding the variation with the surface density scale.

6.2 A Jupiter-mass planet

For completeness we briefly consider the case of a Jupiter-mass planet. The setup is the same as the previous section (with $\Sigma_0 = 7$). The planet potential is switched on over five orbits. Fig. 20 compares the migration curves $a(t)$ for $M_\mathrm{p} = 10^{-3}$ in inviscid and viscous

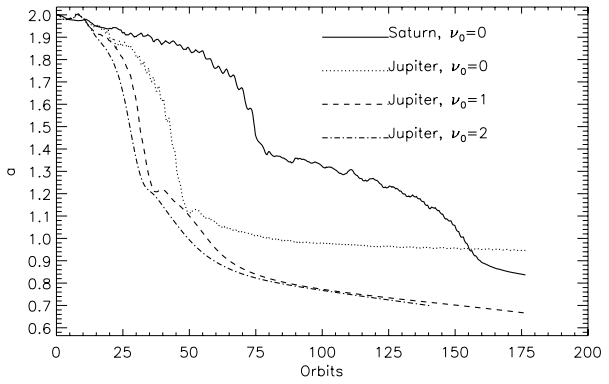

Figure 20. Vortex-induced migration for a Jupiter-mass planet in an inviscid disc (dotted line) and viscous disc ($\nu_0 = 1$, dashed line; $\nu_0 = 2$, dash–dotted line) compared to Saturn-mass planet in a inviscid disc (solid).

($\nu_0 = 1,\ 2$) discs to a Saturn-mass planet in a inviscid disc. The same vortex–planet scattering occurs for the Jupiter-mass inviscid case. This was checked explicitly by examining the vortensity evolution and observing a vortex associated with the inner gap edge buildup and flowing across the co-orbital region. Jupiter induces stronger shocks and therefore higher amplitude vortensity rings, so they are more unstable. The instability growth time-scale is therefore shorter than that of Saturn, so the vortex-induced migration occurs very soon after the planet in introduced.

The $a(t)$ for Jupiter in an inviscid disc shows two migration phases – fast and slow – and that significant orbital decay occurs within $\sim 50P_0$. These features were also observed by Pepliński et al. (2008b). However, the fast phase of Pepliński et al. is almost a linear function of time, whereas in our inviscid case migration is clearly accelerating inwards during $t \lesssim 50P_0$. In our case, there is an abrupt transition to the slow phase whereas that of Pepliński et al. is smoother and no vortices were identified. Although Pepliński et al. did not include physical viscosity, their Cartesian code is more diffusive and vortex formation is suppressed (de Val-Borro et al. 2007). In the late stages of the inviscid case, thin vortensity rings reform and inhibit further migration. A new vortex develops at this stage but it does not grow a sufficient size to induce another episode within simulation time. This growth is limited by the availability of mass being reduced because of proximity to the inner boundary. We remark that inward migration is also inhibited as the planet approaches the inner boundary due to lack of availability of mass in the work of Pepliński et al.. None the less the fast migration phase is more extensive than in the Saturn-mass case because of the stronger perturbation.

Interestingly, adopting a standard viscosity $\nu_0 = 1$ results in a similar behaviour for the fast migration phase, though the transition to slow migration is smoother than for zero viscosity. The vortensity distribution for $\nu_0 = 1$ is also much smoother than for $\nu_0 = 0$ and individual vortices were not identified for the inner gap edge. This is consistent with de Val-Borro et al. (2007) who showed that $\nu = \mathrm{O}(10^{-5})$ suppresses vortex formation. With $\nu_0 = 1$, flow through the co-orbital region is a smoother function of time, unlike episodic behaviour of inviscid discs, and therefore the planet does not experience sudden stalling.

A case with $\nu_0 = 2$ is also shown in Fig. 20. The orbital decay time-scale is again $\sim 50P_0$, consistent with type III migration. The transition from fast to slow migration is again smoothed (cf. $\nu_0 = 0,\ 1$), the fast phase is now less abrupt and qualitatively closer to that found by Pepliński et al. (2008b). These results indicate that our inviscid cases have lower effective viscosity than that operating in the work of Pepliński et al.

7 SUMMARY AND DISCUSSION

In this paper, we have studied the role of large-scale vortices in type III migration in low-viscosity discs. We focused mainly on Saturn-mass planets because they open partial gaps, a configuration where type III migration can operate if the disc is massive (Masset & Papaloizou 2003). Type III migration would occur when the planet is Saturn mass before growing to Jovian mass. We first demonstrated through numerical simulations and semi-analytic modelling of inviscid discs that vortensity rings originate from spiral shocks induced by the planet. For Saturn or more massive planets, the rings reside just inside the co-orbital region, while for less massive planets they are not co-orbital features. Vortensity rings are set up independent of whether the planet is introduced suddenly or gradually over several orbits. A Jupiter-mass planet introduced in the latter manner, that was held on a fixed circular orbit, was considered by de Val-Borro et al. (2007). They found vortex formation at gap edges for small enough imposed viscosity. We remark that this instability occurs independent of the disc mass so it is expected to occur also for low-viscosity slow type II migration. But, as this type of migration does not involve significant coorbital flow, the vortex–planet interactions described in this paper, that operate for fast migration, are not expected. This is found to be the case when slow migration phases occur in the work presented here.

We also found that for a migrating Saturn-mass planet gap edges, associated with local vortensity minima, are dynamically unstable to non-axisymmetric perturbations. Dominant unstable modes are localized go on to develop into vortices which merge in the non-linear regime, as verified by simulations. The effect of vortices on migration is most significant in low-viscosity discs ($\nu \lesssim 0.25 \times 10^{-5}$) because the instability is suppressed at higher viscosity. In the inviscid limit, we estimate that only a small numerical viscosity is present and much smaller than an imposed physical viscosity of $\nu = \mathrm{O}(10^{-6})$. However, a viscosity of that magnitude is unable to suppress the instability. Thus, our conclusions should be unaffected by numerical viscosity. The presence of high density vortices at the gap edge produces non-smooth migration, with episodes of fast migration corresponding to the vortex–planet interaction. This is analogous to planet–planet scattering, and the planet's orbital radius jumps by a few Hill radii in one episode. The vortex is also responsible for stalling migration in discs with initially flat surface density. In this case, there can be repeated episodes of vortex-induced migration. Viscosity smooths the flow across the co-orbital radius, but has limited effect on the extent of orbital decay via the type III mechanism.

We also explored the role of vortices in inviscid discs of different masses. The extent of orbital decay in a single episode of fast migration is independent of initial surface density scaling. This suggests a critical vortex mass or surface density is required to interact, which can be linked to the concept of the co-orbital mass deficit that drives type III migration. The case of a Jupiter-mass planet in an inviscid disc also displayed vortex–planet interaction.

7.1 Outstanding issues

One issue not considered in detail in this paper are boundary effects, although we used the damping boundary conditions (de Val-Borro et al. 2006) which is aimed to remove reflections. The instabilities

that lead to vortex development are localized near gap edges. As long as the planet, and hence vortex formation, is far from the disc edges, boundary effects on vortex–planet interaction should be limited. We have run a simulation with a Saturn-mass planet, where the domain is expanded to $r = [0.2, 6.0]$ and compared $a(t)$ to the fiducial disc which occupies $r = [0.4, 4.0]$. The extended domain case still exhibited non-smooth $a(t)$ with similar orbital decays during the first two episodes of rapid migration. As the domain was extended inwards, there was a third phase of rapid migration which is readily understood on account of the greater availability of mass at small radii. Boundary effects should be examined in more detail in future work, but should not change the main conclusion of this paper, which is that in a low-viscosity disc type III migration is induced by vortices and episodic.

Although we have demonstrated the effect of vortices on migration, it is natural to question their existence as long-lived structures in real discs with finite viscosity. Recently, Li et al. (2009) studied migration in nearly laminar discs in the type I regime. They found effects at low viscosity, which tend to slow down migration, begin to appear for $\nu \leq 10^{-7}$. Their simulations last $O(10^3)$ orbits. In our case, non-smooth migration can be observed at $\nu = O(10^{-6})$. We adopted a more massive planet so vortex formation occurs quickly, and since type III migration time-scales are much shorter than type I a very small viscosity is not required in order to allow the development of sharp features in the disc (which the instability relies on). Vortices can thus interfere with migration when viscosity is one order of magnitude smaller than the standard value $\nu = 10^{-5}$.

We have used the simplest model and numerical setup to describe the disc–planet system. One physical issue is the lack of inclusion of self-growity (SG). It may be important when discussing type III migration since this operates in massive discs (Masset & Papaloizou 2003). In order to have self-consistent physics, SG is essential. Although Li et al. (2009) included SG, its role was not discussed. The effect of self-gravitating vortices on the migration of the larger mass planets considered here should be explored. We note in the standard viscous disc with $\nu = 10^{-5}$ vortices are transient features. However, it is conceivable that SG may mitigate the effects of viscous diffusion because vortices have high surface density. Thus, vortices may exist for higher viscosity values in discs with SG. These issues will be the subject of a future study.

REFERENCES

Artymowicz P., 2004a, in Caroff L., Moon L. J., Backman D., Praton E., eds, ASP Conf. Ser. Vol. 324, Debris Disks and the Formation of Planets. Astron. Soc. Pac., San Francisco, p. 39

Artymowicz P., 2004b, KITP Conference: Planet Formation: Terrestrial and Extra Solar Migration Type III, Power Point presentation

Balmforth N. J., Cunha M. S., Dolez N., Gough D. O., Vauclair S., 2001, MNRAS, 323, 362

D'Angelo G., Bate M. R., Lubow S. H., 2005, MNRAS, 358, 316

de Val-Borro M. et al., 2006, MNRAS, 370, 529

de Val-Borro M., Artymowicz P., D'Angelo G., Peplinski A., 2007, A&A, 471, 1043

Goldreich P., Tremaine S., 1979, ApJ, 233, 857

Goldreich P., Tremaine S., 1980, ApJ, 241, 425

Kevlahan N.-R., 1997, J. Fluid Mech., 341, 371

Koller J., Li H., Lin D. N. C., 2003, ApJ, 596, L91

Korycansky D. G., Papaloizou J. C. B., 1995, MNRAS, 274, 85

Li H., Finn J. M., Lovelace R. V. E., Colgate S. A., 2000, ApJ, 533, 1023

Li H., Colgate S. A., Wendroff B., Liska R., 2001, ApJ, 551, 874

Li H., Li S., Koller J., Wendroff B. B., Liska R., Orban C. M., Liang E. P. T., Lin D. N. C., 2005, ApJ, 624, 1003

Li H., Lubow S. H., Li S., Lin D. N. C., 2009, ApJ, 690, L52

Lin D. N. C., Papaloizou J., 1986, ApJ, 309, 846

Lovelace R. V. E., Li H., Colgate S. A., Nelson A. F., 1999, ApJ, 513, 805

Lynden Bell D., Pringle J. E., 1974, MNRAS, 168, 603

Masset F., 2000a, A&AS, 141, 165

Masset F. S., 2000b, in Garzón G., Eiroa C., de Winter D., Mahoney T. J., eds, ASP Conf. Ser. Vol. 219, Disks, Planetesimals, and Planets. Astron. Soc. Pac., San Francisco, p. 75

Masset F. S., 2002, A&A, 387, 605

Masset F. S., Papaloizou J. C. B., 2003, ApJ, 588, 494

Mayor M., Queloz D., 1995, Nat, 378, 355

Ou S., Ji J., Liu L., Peng X., 2007, ApJ, 667, 1220

Paardekooper S.-J., Papaloizou J. C. B., 2009, MNRAS, 394, 2297

Paardekooper S., Baruteau C., Crida A., Kley W., 2010, MNRAS, 401, 1950

Papaloizou J. C. B., 2005, Celes. Mech. Dynamical Astron., 91, 33

Papaloizou J. C. B., Lin D. N. C., 1989, ApJ, 344, 645

Papaloizou J. C. B., Pringle J. E., 1984, MNRAS, 208, 721

Papaloizou J. C. B., Pringle J. E., 1985, MNRAS, 213, 799

Papaloizou J. C. B., Pringle J. E., 1987, MNRAS, 225, 267

Papaloizou J. C. B., Terquem C., 2006, Rep. Prog. Phys., 69, 119

Papaloizou J. C. B., Nelson R. P., Snellgrove M. D., 2004, MNRAS, 350, 829

Papaloizou J. C. B., Nelson R. P., Kley W., Masset F. S., Artymowicz P., 2007, in Reipurth B., Jewitt D., Keil K., eds, Protostars and Planets V. Univ. Arizona Press, Tucson, p. 655

Pepliński A., Artymowicz P., Mellema G., 2008a, MNRAS, 386, 164

Pepliński A., Artymowicz P., Mellema G., 2008b, MNRAS, 386, 179

Pepliński A., Artymowicz P., Mellema G., 2008c, MNRAS, 387, 1063

Press W. H., Teukolsky S. A., Vetterling W. T., Flannery B. P., 1992, Numerical Recipes in FORTRAN: The Art of Scientific Computing, 2nd edn. Cambridge Univ. Press, Cambridge

Stone J. M., Norman M. L., 1992, ApJS, 80, 753

Tanaka H., Takeuchi T., Ward W. R., 2002, ApJ, 565, 1257

Ward W. R., 1997, Icarus, 126, 261

APPENDIX A: UPPER LIMIT ON THE HORSESHOE WIDTH

We deduce an upper limit on the horseshoe width x_s that is valid in the limit of either zero or constant pressure. Consider a local Cartesian frame that has origin at the planet and hence co-rotates with it with the Keplerian angular velocity $\Omega_p = \sqrt{GM_*/r_p^3}$. Here, M_* is the mass of the central object and r_p is the orbital radius of the planet. In this frame, fluid elements approach the planet from $(x = x_0 > 0,\ y = \infty)$ with velocity $(0, -3\Omega_p x_0/2)$. Suppose such a fluid element executes a horseshoe turn crossing the co-orbital radius at $q = (0, y)$ with velocity $(v_x, 0)$.

We wish to determine an upper bound on the value of x_0 for which such motion occurs. The equation of motion governing a fluid element or particle is

$$\frac{\mathrm{D}\boldsymbol{v}}{\mathrm{D}t} + 2\Omega_p \hat{\boldsymbol{z}} \wedge \boldsymbol{v} = -\nabla\Phi_{\mathrm{eff}}, \tag{A1}$$

where

$$\Phi_{\mathrm{eff}} = -\frac{GM_p}{\sqrt{x^2+y^2}} - \frac{3}{2}\Omega_p^2 x^2. \tag{A2}$$

Here, the *effective potential* Φ_{eff} contains contributions from the gravitational potential of the planet of mass M_p and the tidal potential associated with the central object.

From equation (A1), it follows that the Jacobi invariant

$$J = \frac{1}{2}\boldsymbol{v}^2 + \Phi_{\mathrm{eff}} \tag{A3}$$

is constant along a particle path. Equating J evaluated at $(x, y) = (x_0, \infty)$ to J evaluated at q gives

$$-\frac{3}{8}\Omega_{\rm p}^2 x_0^2 = \frac{1}{2}v_x^2 - \frac{GM_{\rm p}}{y}. \tag{A4}$$

The steady-state Euler equation of motion for v_y evaluated at q is

$$v_x \partial_x v_y + 2\Omega_{\rm p} v_x = -GM_{\rm p}/y^2. \tag{A5}$$

Since in the neighbourhood of q for the type of streamline we consider, $v_x < 0$ and $\partial_x v_y < 0$ we deduce that

$$|v_x| > \frac{GM_{\rm p}}{2\Omega_{\rm p} y^2}. \tag{A6}$$

Combining equations (A4) and (A6), we find that

$$-\frac{3}{8}\Omega_{\rm p}^2 x_0^2 > \frac{1}{2}\left(\frac{GM_{\rm p}}{2\Omega_{\rm p} y^2}\right)^2 - \frac{GM_{\rm p}}{y}. \tag{A7}$$

Writing $x_0 = \hat{x}_0 r_{\rm h}$, where the Hill radius $r_{\rm h} = (M_{\rm p}/(3M_*))^{1/3} r_{\rm p}$ and similarly setting $y = \hat{y} r_{\rm h}$ we obtain

$$\hat{x}_0 < \sqrt{\frac{8}{\hat{y}} - \frac{3}{\hat{y}^4}} \lesssim 2.3. \tag{A8}$$

Thus, because the maximum possible value of the RHS of the above is 2.3, we deduce that particles executing a U-turn could not have originated further than $2.3 r_{\rm h}$. This is comparable to the value of $2.5 r_{\rm h}$ that has been estimated from hydrodynamic simulations (Artymowicz 2004b; Paardekooper & Papaloizou 2009).

APPENDIX B: VORTICITY JUMP ACROSS A STEADY ISOTHERMAL SHOCK

Consider an isothermal shock that is stationary in a frame rotating with angular velocity $\Omega_{\rm p}\hat{\boldsymbol{z}}$. In order to evaluate the vorticity jump across the shock, it is convenient to use a 2D orthogonal coordinate system (x_1, x_2) defined in the disc mid-plane such that one of the curves $x_2 =$ constant $= x_s$ coincides with the shock. The curves $x_1 =$ constant will then be normal to the shock where they intersect it. In addition, the coordinates are set up so that (x_1, x_2, z) is a right-handed system. The $\hat{\boldsymbol{z}}$-component of relative vorticity ω_r can then be written as

$$\omega_r = \frac{1}{h_1 h_2}\left[\frac{\partial(u_2 h_2)}{\partial x_1} - \frac{\partial(u_1 h_1)}{\partial x_2}\right], \tag{B1}$$

where (h_1, h_2) are the components of the coordinate scalefactor.

We note that on $x_2 = x_s$, u_1 is the velocity tangential to the shock. The normal component u_2 and other state variables undergo a jump from pre-shock values to post-shock values on normally traversing the curve $x_2 = x_s$. For an isothermal shock,

$$\frac{u_{2,\rm post}}{u_2} = M^{-2} = \frac{\rho}{\rho_{\rm post}}, \tag{B2}$$

where $M = u_2/c_s$ is the pre-shock perpendicular Mach number, and here and in similar expressions below connecting pre-shock and post-shock quantities we have denoted post-shock values with a subscript post while leaving pre-shock quantities without a corresponding subscript.

Thus the jump in relative vorticity is

$$[\omega_r] = \omega_{r,\rm post} - \omega_r. \tag{B3}$$

Quite generally, the x_1 component of the equation of motion for a steady-state flow is

$$\frac{u_1}{h_1}\frac{\partial u_1}{\partial x_1} + \frac{u_2}{h_2}\frac{\partial u_1}{\partial x_2} - u_2\left(\frac{u_2}{h_1 h_2}\frac{\partial h_2}{\partial x_1} - \frac{u_1}{h_1 h_2}\frac{\partial h_1}{\partial x_2}\right) = -\frac{1}{\rho h_1}\frac{\partial P}{\partial x_1} - \frac{1}{h_1}\frac{\partial \Phi}{\partial x_1} + 2\Omega_{\rm p} u_2, \tag{B4}$$

or equivalently

$$\frac{u_1}{h_1}\frac{\partial u_1}{\partial x_1} + \frac{u_2}{h_1}\frac{\partial u_2}{\partial x_1} - (2\Omega_{\rm p} + \omega_r)u_2 = -\frac{1}{\rho h_1}\frac{\partial P}{\partial x_1} - \frac{1}{h_1}\frac{\partial \Phi}{\partial x_1}, \tag{B5}$$

where P is the pressure and Φ the total potential (the latter quantity being continuous across the shock). From (B5) we obtain an expression for the relative vorticity in the form

$$\omega_r = \frac{1}{h_1}\frac{\partial u_2}{\partial x_1} + \frac{u_1}{u_2 h_1}\frac{\partial u_1}{\partial x_1} + \frac{1}{\rho u_2 h_1}\frac{\partial P}{\partial x_1} + \frac{1}{u_2 h_1}\frac{\partial \Phi}{\partial x_1} - 2\Omega_{\rm p}. \tag{B6}$$

Applying equation (B6) to give an expression for the post shock relative vorticity, and using equation (B2) to express the post-shock normal velocity and density in terms of the corresponding pre-shock quantities, the vorticity jump can be written in the form

$$[\omega_r] = \frac{1}{h_1}\frac{\partial(M^{-2}u_2)}{\partial x_1} + \frac{M^2 u_1}{u_2 h_1}\frac{\partial u_1}{\partial x_1} + \frac{M^2}{u_2 h_1}\frac{\partial \Phi}{\partial x_1} + \frac{1}{\rho u_2 h_1}\frac{\partial P_{\rm post}}{\partial x_1} - (\omega_r + 2\Omega_{\rm p}). \tag{B7}$$

Adopting a locally isothermal equation of state, we have $P_{\rm post} = M^2 P$. Substituting this into equation (B7), while making use of equation (B6) together with the relation $u_2 = c_s M$, we obtain

$$[\omega_r] \equiv [\omega] = -\frac{c_s(M^2-1)^2}{M^2 h_1}\frac{\partial M}{\partial x_1} + (M^2-1)\omega - \frac{(M^4-1)}{M h_1}\frac{\partial c_s}{\partial x_1}, \tag{B8}$$

where $\omega = 2\Omega_{\rm p} + \omega_r$ is the absolute vorticity.

Setting $h_1 {\rm d}x_1 = {\rm d}S$ with ${\rm d}S$ being the corresponding element of distance measured parallel to the shock, this takes the form

$$[\omega_r] \equiv [\omega] = -\frac{c_s(M^2-1)^2}{M^2}\frac{\partial M}{\partial S} + (M^2-1)\omega - \frac{(M^4-1)}{M}\frac{\partial c_s}{\partial S}. \tag{B9}$$

This gives the vorticity jump across a shock in terms of pre-shock quantities measured in the rotating frame in which it appears steady. It is important to note that the expression (B9) applies specifically in the right-handed coordinate system we have adopted with shock location given by $x_2 = x_s$. If we instead adopt $x_1 = x_s$ for this location, the signs of the derivative terms would be reversed as in the expression (2.23) given in Kevlahan (1997). Note too that the last term on the RHS that is proportional to the gradient of c_s along the shock arises from the assumption of a *locally* isothermal equation of state and is not present in the treatment given by Kevlahan (1997).

This paper has been typeset from a TEX/LATEX file prepared by the author.